Study of dynamical neutral-plasma coupling processes in the low-latitude ionosphere based on ground-based airglow observations

Daisuke Fukushima

Acknowledgements

The author is profoundly grateful to Professor Kazuo Shiokawa of the Solar-Terrestrial Environment Laboratory, Nagoya University (STEL), for his kind support and courteous supervision for the present study.

The author is also deeply grateful to Associate Professor Yuichi Otsuka of the STEL, for his important advice and useful discussions.

The author is indebted to Associate Professor Nozomu Nishitani and Assistant Professor Shin Suzuki of the STEL, for their kind guidance and helpful suggestions.

Special thanks are due to the members of review committee on this thesis, Professor Kazuo Shiokawa, Professor Shinobu Machida, Associate Professor Nozomu Nishitani, Associate Professor Yoshizumi Miyoshi, and Associate Professor Yuichi Otsuka of STEL, Nagoya University, and Associate Professor Akinori Saito of Kyoto University.

The author would like to thank the technicians of the STEL, Mr. Yasuo Katoh, Mr. Mitsugi Satoh, Ms. Yuka Yamamoto, and Mr. Yoshiyuki Hamaguchi for their helpful support of the development and operation of the all-sky imager at Kototabang and the Fabry-Perot interferometer at Kototabang and Chiang Mai.

The author would also like to thank Dr. Minoru Kubota, Dr. Takuya Tsugawa, Dr. Tsutomu Nagatsuma, and Dr. Tatsuhiro Yokoyama of the National Institute of Information and Communications Technology (NICT), for their helpful support of operation of the instruments under the Southeast Asia Low-latitude Ionospheric Network (SEALION) project.

Thanks are also due to Dr. Michi Nishioka of the NICT, for her

cooperation in data analysis.

The author would like to thank all members of the Division 2, STEL, for their kind supports in the daily research life.

The airglow observation at Kototabang was carried out in collaboration with the Research Institute for Sustainable Humanosphere, Kyoto University, Japan, and the National Institute of Aeronautical and Space Science, Indonesia.

The airglow observation at Chiang Mai was carried out in collaboration with the NICT, Japan, and Chiang Mai University, Thailand under the SEALION project.

The ionosonde observations at Kototabang and Chiang Mai were operated by the NICT under the SEALION project.

Equivalent black body temperature (Tbb) data were provided by the Japan Meteorological Agency and are distributed by Kochi University, Japan.

This work was supported by Grant-in-Aid for Scientific Research (13573006, 20244080), on Priority Area (764), and by Strategic Funds for the Promotion of Science and Technology including the IUGONET project of the Ministry of Education, Culture, Sports, Science and Technology, Japan.

Some descriptions of Chapters 1, 2, 3, and 4 are taken from *Fukushima* [2012], *Fukushima et al.* [2012], *Fukushima et al.* [2015].

Abstract

Ionospheric disturbances are caused by atmospheric waves from the lower atmosphere and electromagnetic disturbances from the magnetosphere. The ionospheric disturbances can be an obstacle for satellite radio signal as it propagates from satellite to the ground, causing interference and phase delay of the signal such as that from Global Positioning System (GPS). Thus, investigation of the ionospheric disturbances is important for reliable communication between satellite and ground including their use for positioning. In this thesis, we conducted three studies of neutral-plasma coupling processes associated with ionospheric disturbances at equatorial and low latitudes, i.e., medium-scale traveling ionospheric disturbances (MSTIDs), plasma bubbles, and a midnight brightness wave (MBW), by using nighttime airglow observations.

First, we statistically studied nighttime MSTIDs observed at Kototabang, Indonesia (geographic longitude (GLON): 100.3°E, geographic latitude (GLAT): 0.2°S, and geomagnetic latitude (MLAT): 10.6°S) during a 7-year period from October 2002 to October 2009. MSTIDs were observed in 630-nm nighttime airglow images by using a highly-sensitive all-sky airglow imager. The averages and standard deviations of horizontal phase velocities, periods, and horizontal wavelengths of the MSTIDs during the 7 years were 320±170 m/s, 42±11 min, and 790±440 km, respectively. The occurrence rate of the observed MSTIDs decreased with decreasing solar activity. The average horizontal wavelength of MSTIDs increased with decreasing solar activity. Southward MSTIDs were dominant throughout the 7 years of observations. These facts are consistent with the hypothesis that the observed MSTIDs are caused by gravity waves in the thermosphere.

We also compared the propagation directions of the observed MSTIDs with the locations of tropospheric convection activity for the MSTIDs which could have existed as gravity waves in the lower atmosphere. Strong tropospheric convection were found within ±30 degrees from the source directions of MSTIDs in 81% of the MSTID events for the phase velocities less than 300 m/s (sound speed in the lower atmosphere). In these events, gravity waves were possibly generated from strong convection in the troposphere and directly propagated into the thermosphere.

Second, we firstly report plasma bubbles and thermospheric neutral winds simultaneously observed at Kototabang and Chiang Mai, Thailand (GLON: 98.9°E, GLAT: 18.8°N, and MLAT: 8.9°N), which are nearly geomagnetically conjugate stations. These plasma bubbles were observed in 630-nm nighttime airglow images at both stations, for 7 hours from 13 to 20 UT (from 20 to 03 LT) on 5 April 2011. The bubbles continuously propagated eastward with velocities of 100-125 m/s. The 630-nm images at Chiang Mai and those mapped to the conjugate point of Kototabang fit very well, which indicates that the observed plasma bubbles were geomagnetically connected. The eastward thermospheric neutral winds measured by two Fabry-Perot interferometers were 70-130 m/s at Kototabang and 50-90 m/s at Chiang Mai. We compared the observed plasma bubble drift velocity with the velocity calculated from the observed neutral winds and the model conductivity, to investigate the F-region dynamo contribution to the plasma drift. The estimated drift velocities were 60-90% of the observed velocities of the plasma bubbles, suggesting that the thermospheric zonal wind velocities mostly dominate the plasma drift velocities through the F-region dynamo effect.

Finally, we conducted geomagnetically conjugate observations of 630-nm airglow for an MBW at Kototabang and Chiang Mai. An airglow enhancement which is considered to be an MBW was observed in 630-nm airglow images at Kototabang around local midnight from 1540 to 1730 UT (from 2240 to 0030 LT) on 7 February 2011. This

MBW was propagating south-southwestward, which is geomagnetically poleward, with a velocity of 290 m/s. However, similar wave was not observed in the 630-nm airglow images at Chiang Mai. This is the first evidence that an MBW does not have geomagnetic conjugacy. We simultaneously observed thermospheric neutral winds observed by a co-located Fabry-Perot interferometer at Kototabang. The observed meridional winds turned from northward (geomagnetically equatorward) to southward (geomagnetically poleward) just before the wave was observed. This result suggests that the observed MBW was generated by the poleward winds which push ionospheric plasma down along geomagnetic field lines and thereby the 630-nm airglow intensity was enhanced. The bottomside ionospheric heights observed by ionosondes rapidly decreased at Kototabang and slightly increased at Chiang Mai. We discuss the possibility that the polarization electric field inside the observed MBW is projected to the northern hemisphere causing the observed height increases at Chiang Mai.

The results of these three studies indicate that atmospheric gravity waves and thermospheric neutral winds mainly contribute to the ionized atmosphere and give complicated variations to the ionospheric plasma. We conclude that the effects of the neutral atmosphere in the thermosphere play dominant roles to create various characteristics of ionospheric disturbances through neutral-plasma coupling processes at equatorial and low latitudes.

Contents

Chapter 1

Introduction

1.1 Structure of Earth's atmosphere

The Earth's atmosphere is classified into four regions vertically based on the temperature variations. They are categorized from lower to upper as troposphere, stratosphere, mesosphere, and thermosphere. The left part in Figure 1.1 shows typical profiles of the Earth's atmospheric temperature for neutral gas [*Kelley*, 2009].

The troposphere is the lowest region in the Earth's atmosphere at altitudes of ∼0-10 km. In the troposphere, temperatures decrease linearly with increasing altitudes. A variety of meteorological phenomena occur in the troposphere. Disturbances occurred in this region sometimes propagate to and affect the upper atmosphere. Boundary between the troposphere and the stratosphere is called as tropopause.

The stratosphere is the region at altitudes of ∼10-50 km. The main feature of the stratosphere is that the temperatures increase with increasing altitudes. In this region, the meteorological disturbances do not frequently occur compared to the troposphere. An ozone layer exists in the stratosphere and absorbs ultraviolet rays from the sun to produce local temperature maximum at stratopause.

The mesosphere is the region at altitudes of ∼50-90 km. The temperatures decrease with increasing altitudes. Atmospheric waves such as gravity waves, tidal waves, and planetary waves generated from the lower atmosphere exist in

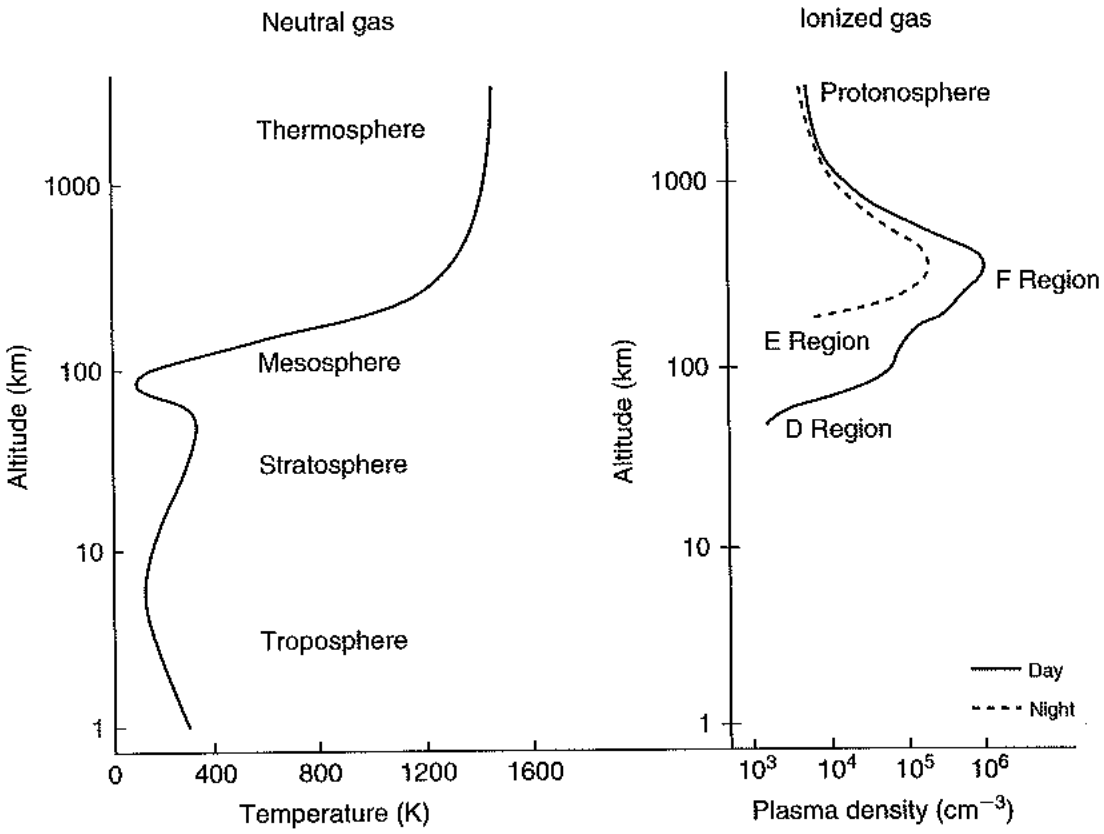

Figure 1.1: Typical profiles of neutral atmospheric temperature and ionospheric plasma density (reproduced from *Kelley* [2009]).

the mesosphere. These atmospheric waves significantly disturb the mesosphere. Boundary between the mesosphere and the thermosphere is called as mesopause. In the mesopause at an altitude of ∼90 km, the temperature is lowest (∼180 K) in the Earth's atmosphere.

The thermosphere is the region at altitudes of ∼90-1000 km. Above the mesopause region, the temperatures excessively increase from 200 to 1000-2000 K. The temperatures in the thermosphere vary with ∼11-year solar activities. A part of the neutral particles are ionized by X-rays and ultraviolet rays from the sun, forming the ionosphere.

1.2 Ionosphere

The region in the thermosphere with ionized gas is called as ionosphere. In the ionosphere, plasma is continuously lost due to recombination between ions and electrons as well as it is produced by solar radiation. The ion and electron density is at most ∼0.1 % of the neutral density. Thus, the neutral component and motion is dominant for determining the ionospheric structures. The plasma is transported in the ionosphere by gravity force, pressure gradient, electromagnetic force, and collision with neutral particles.

The right part in Figure 1.1 shows the ionospheric plasma density. Inside of the ionosphere is classified into three regions, as D region (altitudes of 80-100 km), E region (100-150 km), and F region (above 150 km). In the bottomside of the F region, plasma density monotonously increases with altitudes, considering only the ratio of production and loss rates of oxygen ions (O^+) which are major ion species in the F region. In the topside of the F region, however, the plasma density decreases with altitudes due to ambipolar diffusion. As a result, the F-region peak, where the plasma density is maximum, is located at an altitude of ∼300 km. At this altitude, various dynamic variations occur through ion-neutral collisions.

Various plasma phenomena exist in the ionospheric F region, such as traveling ionospheric disturbances (TIDs), plasma bubbles, and field-aligned irregularities (FAIs). These phenomena interfere with Global Positioning System (GPS) radio signals which pass through the ionosphere. They also interfere with high-

frequency (HF) radio-wave communications because they use reflection by the ionosphere for long-distance communication. Investigating the ionospheric environment is important from these reasons.

1.3 Airglow emission

At altitudes above ∼85 km in the thermosphere/ionosphere and the mesopause region, nocturnal airglow emissions originated from atoms and molecules in the atmosphere exist. The emissions are feeble and unable to be recognized with the naked eye. Their maximum intensity is in the order of hundred Rayleighs per one emission line at most.

Figure 1.2 shows an example of nighttime airglow spectrum obtained by an airglow spectrograph [*Johnston and Broadfoot*, 1993]. Typical airglow emissions are OI (wavelength of 557.7 nm and emission altitude of ∼96 km), OI (630.0 nm, ∼200-300 km), Na-D (589.3 nm, ∼90 km), and OH Meinel bands (550 nm-4.4 μm, ∼86 km). These emission layers exist at nearly fixed altitudes. Thus, the horizontal structures in the atmosphere and the thermosphere at these altitudes of emission layers can be investigated by taking images of these airglow emissions.

The airglow imaging technique has been used in highly sensitive all-sky imagers with back-illuminated cooled charge-coupled device (CCD) cameras since the late 1990s to observe dynamic variations of the thermosphere, ionosphere, and mesopause region. The OI (630.0-nm) emission layer is located at altitudes of ∼200-300 km at the bottom of the F region. The chemical reactions that generate the 630-nm airglow emission are

$$O^+ + O_2 \longrightarrow O_2^+ + O, \tag{1.1}$$

$$O_2^+ + e^- \longrightarrow O(^1D) + O, \tag{1.2}$$

and

$$O(^1D) \longrightarrow O(^3P) + h\nu_{630.0nm}. \tag{1.3}$$

The amount of 630-nm emissions is proportional to a product of the density of molecular oxygen (O_2) and the density of O^+ because reaction (1.1) dominates

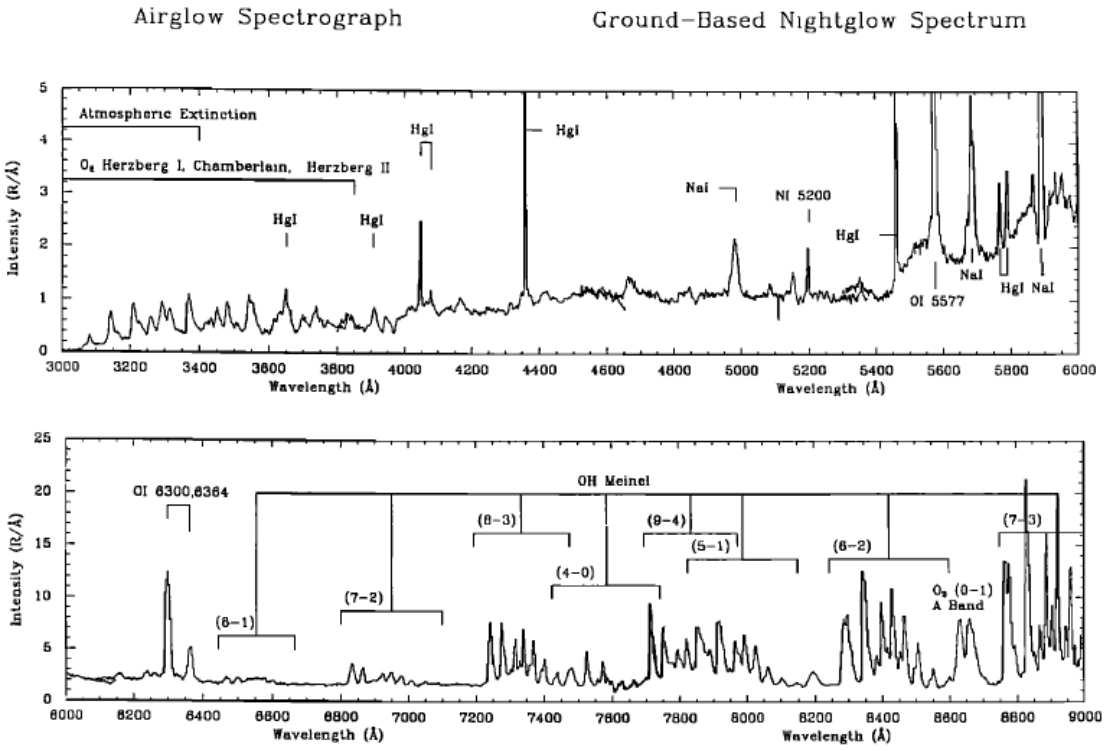

Figure 1.2: The nighttime airglow spectrum from an airglow spectrograph (reproduced from *Johnston and Broadfoot* [1993])

the whole process. In the F region, the O^+ density is nearly equal to the electron density. Thus, 630-nm airglow intensity is a sensitive indicator of F-region plasma density which shows much faster and finer scale dynamic variations than the O_2 density does [e.g., *Sobral et al.*, 1993]. If the height of the F region decreases, the 630-nm airglow intensity increases, because the O^+ reacts with high-density O_2 at lower altitudes. Thus, the 630-nm airglow intensity is also sensitive to the F-region height variations.

1.4 Medium-scale traveling ionospheric disturbances

Medium-scale traveling ionospheric disturbances (MSTIDs) are electron density variations propagating in the ionosphere. MSTIDs have horizontal wavelengths of ∼100-1000 km and periods of ∼15-60 min [*Hunsucker*, 1982]. MSTIDs have been observed by radio wave techniques such as ionosonde [e.g., *Bowman*, 1990], HF Doppler [e.g., *Waldock and Jones*, 1986], and ground radars [e.g., *Oliver et al.*, 1995]. From these observations, it has been suggested that MSTIDs are caused by gravity waves [*Hines*, 1960; *Hooke*, 1968].

Since the 1990s, all-sky airglow imagers with highly-sensitive cooled CCDs have been widely employed to observe MSTIDs by utilizing OI (630.0-nm) emissions [e.g., *Mendillo et al.*, 1997; *Taylor et al.*, 1998; *Shiokawa et al.*, 2003]. In Japan, nighttime MSTIDs were observed by using several all-sky airglow imagers in combination [e.g., *Kubota et al.*, 2000; *Saito et al.*, 2001]. By using two all-sky imagers, MSTIDs were simultaneously observed at two geomagnetic conjugate points at middle latitudes [*Otsuka et al.*, 2004]. MSTID observations using the 630-nm airglow have also been carried out at low latitudes in Arecibo, Puerto Rico [e.g., *Garcia et al.*, 2000; *Martinis et al.*, 2010] and in Chile [e.g., *Makela et al.*, 2010]. The phase fronts of these MSTIDs were elongated from northwest to southeast in the northern hemisphere, and southwest to northeast in the southern hemisphere. Such characteristics cannot be explained by the conventional theory of gravity waves [*Miller et al.*, 1997; *Kelley and Miller*, 1997]. Perkins instability has been suggested to play a central role in the growth of these types of MSTIDs

[e.g., *Perkins*, 1973; *Kelley and Fukao*, 1991].

At middle latitudes, MSTIDs have also been observed by using GPS receiver networks [e.g., *Kotake et al.*, 2006, 2007; *Tsugawa et al.*, 2007] and SuperDARN HF radars [e.g., *Ishida et al.*, 2008]. The daytime MSTIDs found through this method were considered to be caused by gravity waves, because their phase fronts were elongated in the east-west direction. Conversely, the nighttime MSTIDs, which had similar features to those observed by airglow imagers, were considered to be caused by plasma instabilities. At Wallops Island, USA, MSTIDs were observed by a Doppler radar system called as TIDDBIT for 6 hours at the bottomside of the F region [*Vadas and Crowley*, 2010]. They showed that these MSTIDs were likely to be gravity waves and propagated in nearly all directions. Hence, from previous observations, gravity waves and plasma instabilities are the two major sources of MSTIDs.

Shiokawa et al. [2006] studied the nighttime equatorial MSTIDs at Kototabang, Indonesia (geographic longitude (GLON): 100.3°E; geographic latitude (GLAT): 0.2°S; and geomagnetic latitude (MLAT): 10.0°S) over 2-year period from October 2002 to October 2004. The majority of the observed MSTIDs had east-west phase fronts and moved southward (poleward). The occurrence of MSTIDs was highest in the pre-midnight hours between May and July. They proposed that, because phase fronts were mostly in the east-west direction, the source of the MSTIDs was gravity waves generated in the lower atmosphere. Such gravity waves oscillate the neutral atmosphere. The north-south motion of the atmosphere move plasma up and down along the geomagnetic field line through ion-neutral collisions. This vertical motion of plasma produces variation in the airglow intensity, as discussed above. Thus, meridionally-moving gravity waves tend to be observed in airglow images. Although *Shiokawa et al.* [2006] have conducted an analysis of MSTIDs at equatorial latitudes, MSTID-dependence on the 11-year solar cycle was not investigated because their observations were limited to 2 years. Therefore, we conduct nighttime MSTID observations over 7 years at equatorial latitudes to find their dependence on solar activities. The results are described in Chapter 3 in detail.

1.5 Plasma bubbles

Plasma bubbles are plasma-density depletions in the ionospheric F region and are generated at equatorial latitudes after sunset. In the Asian longitudinal sector, the occurrence of plasma bubbles is highest in spring and autumn equinoxes [*Burke et al.*, 2004]. The zonal scale size of plasma bubbles varies from several tens to hundreds of kilometers, and their meridional size varies from several hundreds to thousands of kilometers. Plasma bubbles are attributed to the Rayleigh-Taylor instability [e.g., *Kelley*, 2009]. At equatorial latitudes, an eastward electric field at the sunset terminator pushes the F-region plasma upward [e.g., *Farley et al.*, 1986]. Under this condition, a plasma density perturbation at the bottom-side of the F region becomes unstable as a result of the Rayleigh-Taylor instability mechanism. The plasma bubbles develop in the form of field aligned plasma depletions as the low density plasma grows up and rises to higher altitude across the geomagnetic field line [e.g., *Mendillo and Baumgardner*, 1982; *Abdu*, 2001]. Plasma bubbles have been observed in 630-nm airglow images at equatorial and low latitudes as localized airglow depletions [e.g., *Sahai et al.*, 2000; *Abalde et al.*, 2001]. Some airglow-imaging observations show simultaneous plasma bubbles at low- and middle-latitude geomagnetically conjugate points (one northern and one southern) [e.g., *Otsuka et al.*, 2002; *Shiokawa et al.*, 2004; *Sobral et al.*, 2009].

Plasma bubbles usually propagate eastward for several hours. The drift of the plasma bubble is the same as the background plasma drift which corresponds to the $\mathbf{E} \times \mathbf{B}$ drift by the downward perpendicular electric field to the magnetic fields. The electric fields are generated by the background eastward thermospheric winds as a result of the F-region dynamo mechanism. To study the F-region dynamo mechanism, the plasma drift and neutral winds must be observed simultaneously. In the previous study, however, simultaneous observations of plasma bubbles and thermospheric neutral winds were conducted only in one hemisphere. Therefore, we simultaneously observe the plasma bubble and the thermospheric neutral winds at low-latitude conjugate stations in both hemispheres. The results are described in Chapter 4 in detail.

1.6 Midnight brightness waves

The brightness wave is a phenomenon that a region of 630-nm airglow enhancement propagates in meridional directions at low latitudes. The first observation of brightness wave was conducted by *Greenspan* [1966] and *Nelson and Cogger* [1971] in the American longitudinal sector. *Colerico et al.* [1996] observed several brightness wave events by using an all-sky imager at Arequipa, Peru. The brightness waves were observed in the pre-midnight sector (∼20-22 LT) and midnight sector (∼23-01 LT). The earlier brightness wave propagated northward (equatorward) and the later brightness wave propagated southward (poleward). They called these waves pre-midnight brightness wave (PMBW) and midnight brightness wave (MBW), respectively. For these brightness wave events, they observed thermospheric neutral winds and temperature by a Fabry-Perot Interferometer (FPI), and ionospheric heights by an ionosonde. For each instance, the FPI data showed a local minimum in zonal wind and a reversal in meridional winds from equatorward to poleward, and the ionosonde data showed a height decrease in the F region. The observed neutral temperature showed a local maximum which is considered to be the midnight temperature maximum (MTM) [e.g., *Mayr et al.*, 1979]. *Colerico et al.* [1996] suggested a scenario that a pressure bulge accompanying the MTM reverses meridional winds from equatorward to poleward and therefore the poleward winds move F region to lower altitudes along the geomagnetic field to enhance the 630-nm airglow intensity.

The other MBW observations were conducted at Arecibo, Puerto Rico [*Mendillo et al.*, 1997] and Shigaraki, Japan [*Otsuka et al.*, 2003]. The characteristics of these observed MBWs were similar to that reported by *Colerico et al.* [1996]. However, the apparent phase velocity of the MBW observed in Japan (∼500 m/s) was larger than that observed in Peru (∼250-350 m/s) and Puerto Rico (∼300 m/s).

The background thermospheric and ionospheric conditions would contribute to the generation and propagation of the ionospheric disturbances. Several MBW observations by the previous studies suggested that the observed MBW were generated by the poleward neutral winds blowing from the MTM region. However, the conjugate observations have not been conducted for the MBW. Therefore,

we conduct the conjugate airglow observation for the MBW to investigate the geomagnetic conjugacy of the MBW. The results are described in Chapter 5 in detail.

1.7 Purpose of this paper

In this paper, we investigate the coupling process of the dynamics in neutral and ionized atmosphere through the observations of MSTIDs, plasma bubbles, and an MBW at low latitudes, and how neutral-plasma interactions affect the characteristics of these ionospheric disturbances.

In Chapter 2, we describe characteristics of all-sky airglow imagers, FPIs, and ionosondes, which are used in this study.

In Chapter 3, we statistically analyzed 7-year nighttime airglow observation of MSTIDs taken in airglow images at Kototabang, Indonesia, to find their dependence on solar activities. We also compared the MSTID propagation directions with the locations of tropospheric convection activity to find the source of the nighttime MSTIDs observed at low latitudes.

In Chapter 4, we analyzed plasma bubbles and thermospheric neutral winds simultaneously observed at Kototabang and Chiang Mai, Thailand, which are nearly low-latitude geomagnetically conjugate points. We compared the observed plasma bubble velocities and those calculated from the observed neutral wind and modeled ionospheric conductivities, to investigate how the F-region dynamo process affects the plasma drift.

In Chapter 5, we firstly conducted the conjugate airglow observations for an MBW at Kototabang and Chiang Mai, to investigate the geomagnetic conjugacy of the MBW. We also observed the thermospheric neutral winds and ionospheric heights, to investigate their variations accompanied by the MBW at the conjugate points.

In Chapter 6, we summarize these three studies and suggest the importance of neutral-plasma dynamics. We also suggest future studies of the ionospheric disturbances at low latitudes.

Chapter 2

Instrumentation

In this chapter, we introduce three different instruments, all-sky airglow imagers, Fabry-Perot interferometers (FPIs), and ionosondes. We use these instruments in the studies of low-latitude ionospheric disturbances described in Chapters 3, 4, and 5 in detail. We mainly use all-sky imagers to observe the ionospheric disturbances, because their two-dimensional structures can be clearly obtained. FPIs are the unique equipments to observe the thermospheric neutral winds. Ionosondes are a kind of radars to observe the ionospheric heights and peak densities.

2.1 All-sky airglow imager

Nighttime airglow observation has been carried out at Kototabang, Indonesia (GLON: 100.3°E; GLAT: 0.2°S; and MLAT: 10.0°S), by using a highly sensitive all-sky airglow imager. The location of Kototabang is shown in Figure 2.1. The imager (#5) was installed on 26 October 2002 at Kototabang and is one of the Optical Mesosphere Thermosphere Imagers (OMTIs) operated by the Solar-Terrestrial Environment Laboratory (STEL), Nagoya University [*Shiokawa et al.*, 1999; 2009]. We continuously observed nighttime airglow when the moon is below the horizon and the sun is 12° below the horizon. The imager shutter stopped functioning in 2009, and we replaced with a new imager (#13) on 13 June 2010 at Kototabang. The pictures of the imager are shown in Figures 2.2(a) and 2.2(b).

The imagers were equipped with CCDs cooled to a temperature of less than −50 °C and five interference filters that allowed different wavelengths to pass. To observe ionospheric disturbances, we used filters that passed OI (630.0-nm) emissions with bandwidths of 1.6-2.0 nm. Airglow images were acquired at a resolution of 512 × 512 CCD pixels with exposure times of 105-165 s and time resolutions of 270-330 s. The images acquired with the 630-nm filter contain background continuum emissions. To remove the background emissions, we need to measure their intensity at the wavelength where the airglow emission line does not exist. Thus, we selected bandpass filters that passed 572.5-nm light with bandwidths of 1.5-2.1 nm. We assume that the background continuum emissions have a same intensity at 630 nm and 572.5 nm (see, e.g., Figure 1.2). The bandwidths of the filters, exposure times, and time resolutions of each wavelength are shown in Table 2.1.

Another imager was also installed on 24 February 2010 at Sirindhorn Observatory of Chiang Mai University, Chiang Mai, Thailand (GLON: 98.9°E; GLAT: 18.8°N; and MLAT: 8.9°N), which is close to a geomagnetically conjugate point of Kototabang. The location of Chiang Mai is also shown in Figure 2.1. The imager at Chiang Mai has been operated by the National Institute of Information and Communications Technology (NICT) as part of the Southeast Asia Low-latitude Ionospheric Network (SEALION) project [*Kubota et al.*, 2009]. Airglow images were acquired from this imager at a resolution of 512 × 512 CCD pixels with an exposure time of 45 s and a time resolution of 360 s. The bandwidths of the filters, exposure times, and time resolutions of each wavelength are shown in Table 2.1. The geomagnetically conjugate airglow observation at low latitudes become possible by installing the imager at Chiang Mai.

Table 2.1: Parameters of All-Sky Imagers at Kototabang and Chiang Mai

Ch.	Emission	Wavelength	Bandwidth	Exposure	Time resolution
Imager 5			(26 October 2002 - 10 June 2010, at Kototabang)		
1	OI	557.7 nm	1.96 nm	105 s	4.5 min
					5.5 min (After Feb. 2008)
2	OI	630.0 nm	1.98 nm	105 s	4.5 min
				165 s	5.5 min (After Feb. 2008)
3	OH	720-910 nm	190 nm	15 s	4.5 min
					5.5 min (After Feb. 2008)
4	OI	777.4 nm	1.78 nm	165 s	30 min
5	bg	572.5 nm	2.06 nm	105 s	30 min
Imager 13			(13 June 2010 -, at Kototabang)		
1	OI	557.7 nm	1.73 nm	105 s	5.5 min
2	OI	630.0 nm	1.57 nm	165 s	5.5 min
3	OH	>720 nm	–	10 s	5.5 min
4	OI	777.4 nm	1.31 nm	165 s	30 min
5	bg	572.5 nm	1.52 nm	105 s	30 min
Imager operated by NICT			(24 February 2010 -, at Chiang Mai)		
0	Na	589.0 nm	3.1 nm	75 s	6.0 min
1	OI	630.0 nm	3.4 nm	45 s	6.0 min
2	OH	>680 nm	–	15 s	3.0 min
3	OI	777.4 nm	2.8 nm	75 s	6.0 min
4	bg	572.3 nm	2.8 nm	45 s	6.0 min

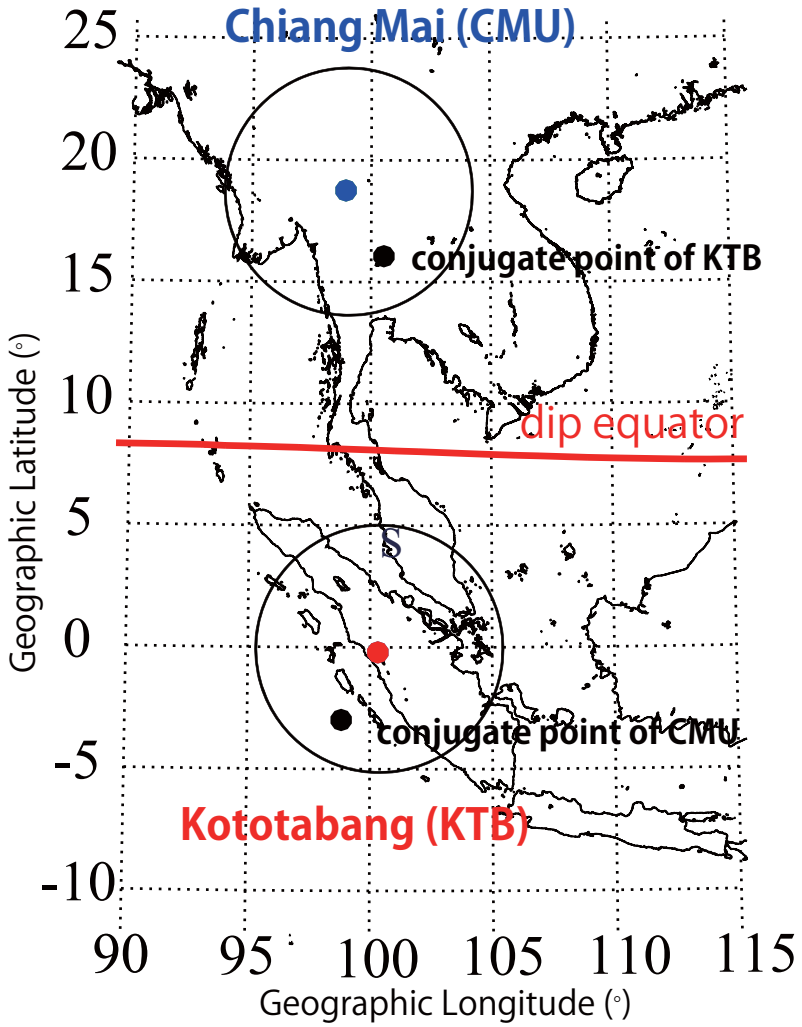

Figure 2.1: Location of Kototabang and Chiang Mai. The geomagnetically conjugate points of these two stations are shown by black dots. The circles show the field-of-view of the all-sky imagers at Kototabang and Chiang Mai.

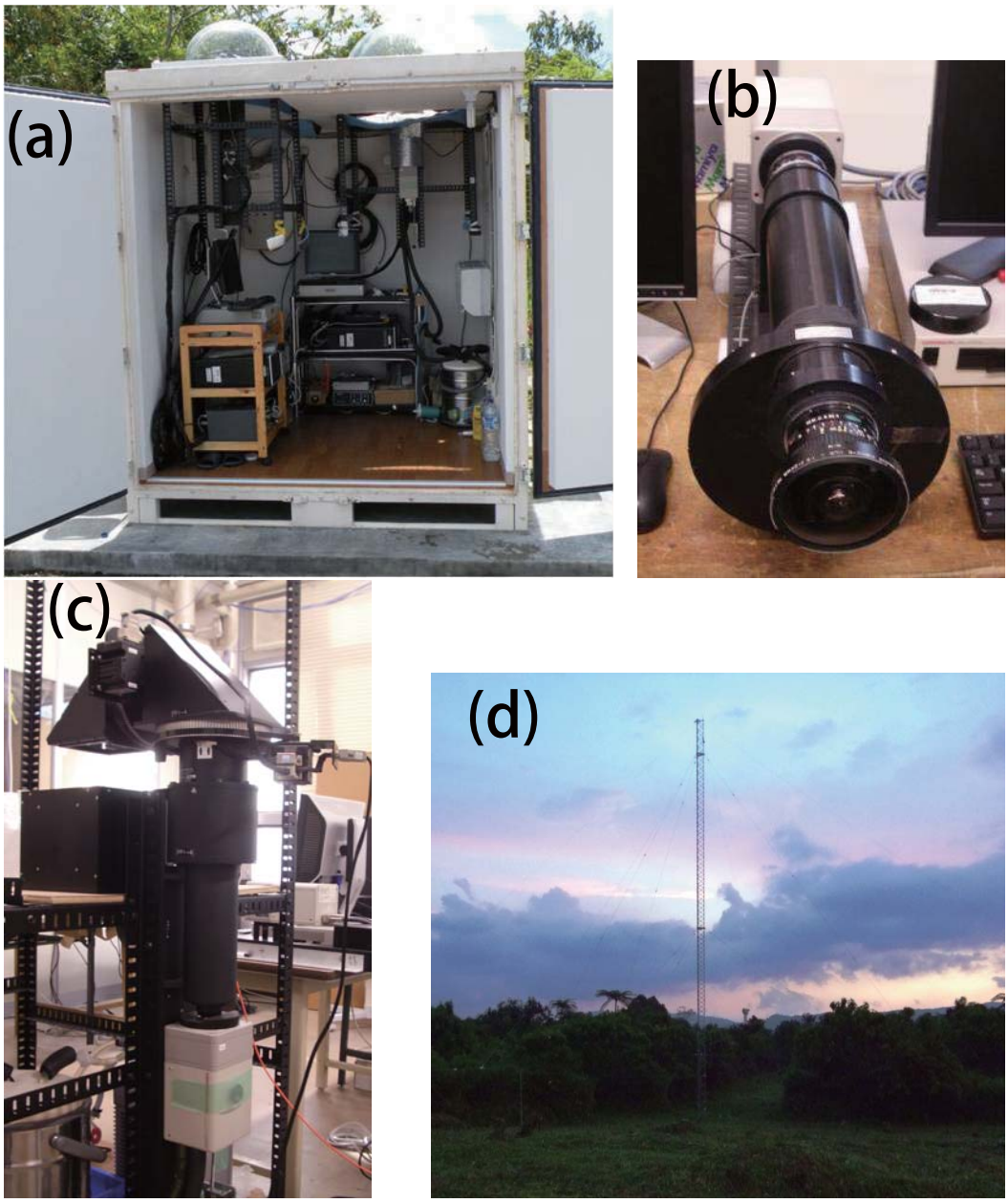

Figure 2.2: (a) Whole picture of a container house at Kototabang with the imager (left side) and the FPI (right side). (b) Body of the imager with the fish-eye lens (front) and the CCD camera (back). (c) Body of the FPI with the sky scanner (top) and the CCD camera (bottom). (d) A picture of the ionosonde.

2.2 Fabry-Perot interferometer

Two identical FPIs were installed, one on 24 February 2010 at Chiang Mai, and one on 13 June 2010 at Kototabang. These FPIs are also part of the OMTIs [*Shiokawa et al.*, 2012] operated by the STEL. The pictures of the FPI are shown in Figures 2.2(a) and 2.2(c). Each FPI used a 70-mm diameter etalon, a CCD cooled to a temperature of −80 °C, and an interference filter that passed 630-nm emissions with a bandwidth of 2.5 nm. A sky scanner was fixed on the top in the FPI, which sequentially scans the 4 directions of north, south, east, and west with an exposure time of 3.5 min for each directions. The airglow entering from the scanner creates interference fringes by passing through the etalon. As a result, 10 interference fringes were taken as 1024×1024 CCD pixel images. The background neutral wind velocity that causes Doppler shift in airglow wavelength can be measured from the shift of these fringe peaks with standard deviations (random errors) of 2-50 m/s. Meridional (zonal) wind velocities are measured from the difference of the Doppler shift between north and south (east and west), as shown in equation (2) of *Shiokawa et al.* [2012]. The time resolution to obtain a meridional and zonal wind vector is 15 min which is one cycle of the sky scanner.

2.3 Ionosonde

Two ionosondes are operated by the NICT as part of the SEALION project at Kototabang and Chiang Mai [*Maruyama et al.*, 2007]. The picture of the ionosonde is shown in Figure 2.2(d). An ionosonde measures ionospheric virtual heights by transmitting radio waves of variable frequencies from ∼2 MHz to higher than 20 MHz. The radio waves transmitted by an ionosonde are reflected by the ionosphere and received on the ground. We can measure the altitudes of the ionosphere from the time delay of the received radio waves. Low-frequency waves are reflected at lower altitudes of the ionosphere where the electron density is low. The plasma density N (m^{-3}) is estimated from the reflected wave frequency f (MHz),

$$N = 1.24 \times 10^{10} \times f^2. \tag{2.1}$$

We use the ionograms which are diagrams of received-wave intensity in the plot of radio-wave frequencies versus time delay that corresponds to the altitudes of wave reflection point. The examples of the ionograms are shown in Figures 2.3(a) and (b), which are simultaneously observed with plasma bubbles on 5 April 2011 and with an MBW on 7 February 2011 at Kototabang, respectively.

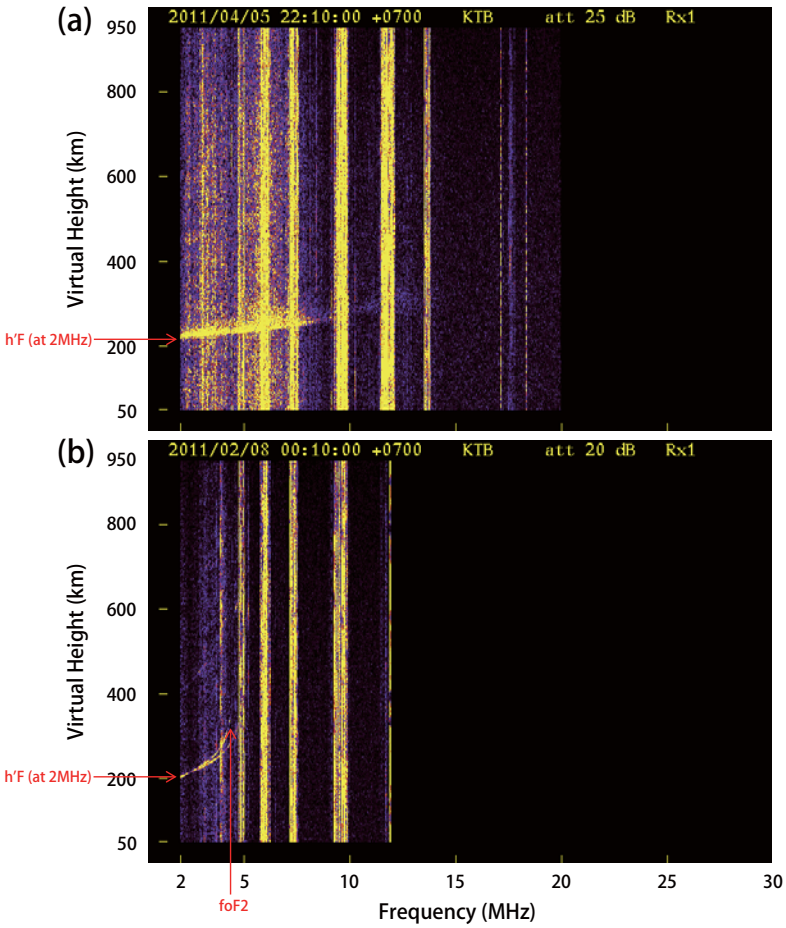

Figure 2.3: Examples of ionograms obtained by an ionosonde at Kototabang (a) at 1510 UT (2210 LT) on 5 April 2011 and (b) at 1710 UT (0010 LT) on 7 February 2011 (8 February 2011 at local time). Virtual heights ($h'F$) at a frequency of 2 MHz and F2-region critical frequency (f_oF_2) are shown by red arrows. The f_oF_2 value on 5 April 2011 could not be measured due to spread of the ionosonde echoes by plasma bubbles.

Chapter 3

Statistical analysis of low-latitude nighttime MSTIDs in 630-nm airglow images over 7 years

Using an all-sky airglow imager at Kototabang, a two-dimensional observation of the MSTIDs has been carried out at low latitudes since October 2002. In south-east Asia including Indonesia, a study of nighttime MSTIDs through the airglow observation was done only by *Shiokawa et al.* [2006]. They found quasi-periodic southward-moving MSTIDs in 630-nm airglow images acquired at Kototabang, Indonesia over 2-year period, from 26 October 2002 to 26 October 2004. They suggested that these observed MSTIDs may be caused by gravity waves in the thermosphere, because phase fronts of the MSTIDs were mostly in an east-west direction. However, the source of the observed MSTIDs have not been identified, since they did not investigate the condition of the lower atmosphere where most of the gravity waves were generated. Moreover, MSTID-dependence on the 11-year solar cycle was not investigated.

In Chapter 3, we analyzed MSTIDs observed in airglow images at Kototabang, Indonesia over a 7-year period from 26 October 2002 to 25 October 2009 to investigate their dependence on solar activity. We also compared the propagation directions of MSTIDs with the locations of tropospheric convection activity to discover the source of the nighttime MSTIDs observed at low latitudes. The

study in Chapter 3 has been reported by *Fukushima et al.* [2012].

3.1 Observations

Figure 3.1 shows a typical example of MSTIDs observed on 9 May 2004 at Kototabang. Figure 3.1(a) shows the variation of airglow intensity from 1210 to 1540 universal time (UT) for a cross section (keogram) of the north-south meridian at the longitude of Kototabang (100.3°E). All-sky coordinates are converted into geographical coordinates in the keogram. Note that the local time (LT) of Kototabang is 7 h ahead of UT. An enhanced airglow region in which the airglow intensity is greater than 400 Rayleigh (R), is seen from 1210 to 1310 UT at geographic latitudes from 5.0°S to 2.0°S. The enhanced region then moves northward from 1.0°N to 5.0°N between 1300 and 1500 UT. This motion from south to north seems to be the equatorward retreat of the equatorial ionization anomaly during nighttime [e.g., *Fejer et al.*, 1991]. The equatorial anomaly, where the high-density F-region plasma exists at low latitudes, is usually located between 10° to 20° north and south of the geomagnetic equator [e.g., *Sagawa et al.*, 2003].

To clearly distinguish the meridional and zonal movements of MSTIDs, we use keograms in airglow intensity deviations. The deviation $\Delta I(t)$ is defined as

$$\Delta I(t) = \frac{I(t) - I_a(t)}{I_a(t)}, \tag{3.1}$$

where $I(t)$ is the airglow intensity at time t and $I_a(t)$ is the average airglow intensity for the interval $t \pm 30$ min.

Figures 3.1(b) and 3.1(c) are meridional and zonal keograms in deviations from the 1-h running averages at the longitude (100.3°E) and latitude (0.2°S) of Kototabang, respectively. In Figure 3.1(b), southward-moving MSTIDs with a period of ∼35 min can be seen from 1230 to 1400 UT in the region where the airglow intensity is greater than ∼200 R. In Figure 3.1(c), we see that MSTIDs move slightly eastward. Therefore, the propagation direction of MSTIDs is categorized as south-southeastward (toward SSE). The horizontal phase velocity of MSTIDs is estimated to be ∼200 m/s from these meridional and zonal keograms.

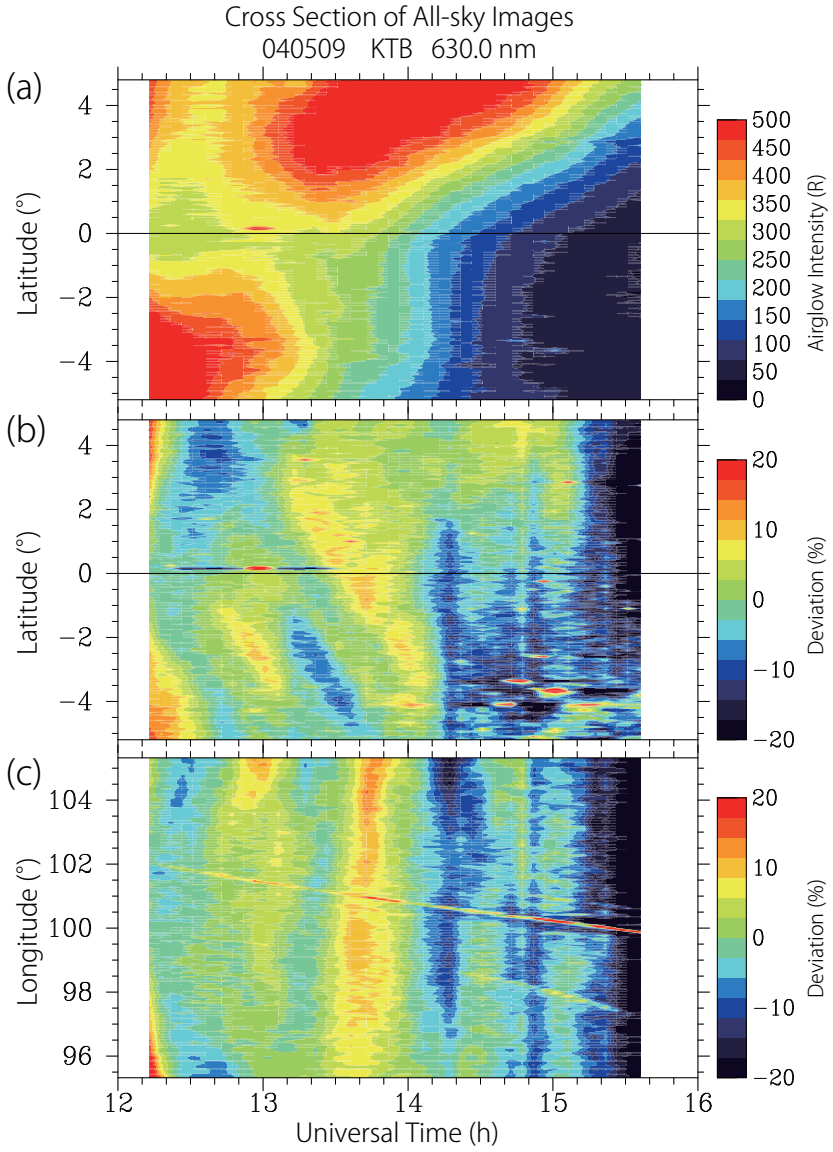

Figure 3.1: Cross sections (keograms) of the 630-nm airglow images observed on 9 May 2004 at Kototabang. (a) Meridional keogram of airglow intensity at the longitude of Kototabang (100.3°E). (b) Meridional keogram in deviations from 1-h running averages at the longitude of Kototabang (100.3°E). (c) Zonal keogram in deviations from 1-h running averages at the latitude of Kototabang (0.2°S).

Figure 3.2 shows 630-nm airglow images acquired from 1312 to 1400 UT in deviations from the 1-h running averages on the same day as in Figure 3.1. An MSTID with an ENE-WSW phase front moving toward the SSE is seen in Figure 3.2. This MSTID corresponds to that seen in Figures 3.1(b) and 3.1(c) from 1300 to 1400 UT.

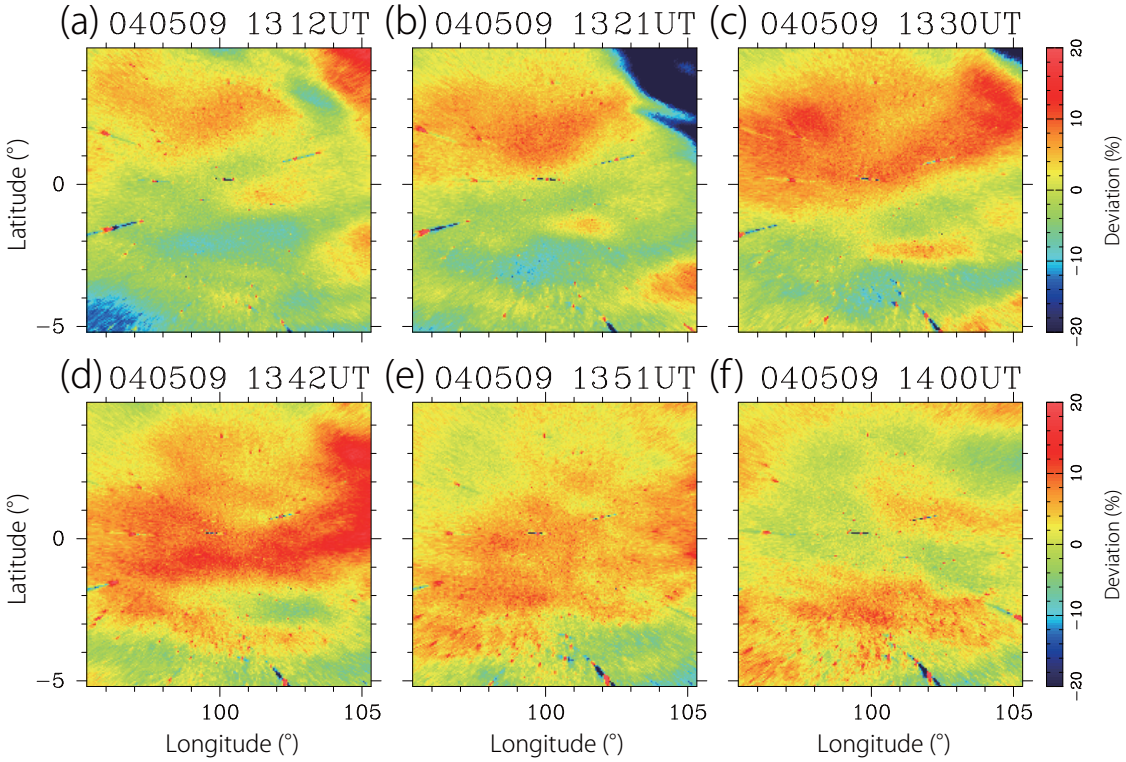

Figure 3.2: The 630-nm airglow images at (a) 1312, (b) 1321, (c) 1330, (d) 1342, (e) 1351, and (f) 1400 UT in deviations from 1-h running averages in geographic coordinates. These images were acquired on the same day as those in Figure 3.1.

3.2 Statistical analysis

We now statistically analyze MSTIDs observed over the 7-year period from 26 October 2002 to 25 October 2009. These MSTIDs were observed in 630-nm airglow images when sky conditions were clear. There were 108 clear-sky nights, totaling 595 clear-sky hours, during the 7 years. Sky conditions from May to July were typically better than in other seasons. Sky conditions in other seasons were clear only on a limited number of nights. In 2002, MSTID observations could not be made due to bad weather. We also note that the imager was out of order due to equipment trouble throughout almost all of June-August 2003, December 2005, July and December 2006, March-April 2007, and March-July 2009. We defined MSTIDs as 630-nm airglow deviations that showed movement in the keograms and as phase fronts in the two-dimensional images of the 630-nm airglow. To differentiate MSTID structures from clouds, we compared the two-dimensional maps and keograms of the 630-nm airglow with those of OH airglow at wavelengths of 720-910 nm. The OH airglow images were acquired with the same imager as for the 630-nm airglow. Since the clouds were found in both the 630-nm and OH images, we could identify MSTID structures as those seen in only the 630-nm images.

Figures 3.3(a)-(c) show the occurrence rates of MSTIDs observed at Kototabang in each year from 2003 to 2009; in the four seasons: February-April, May-July, August-October, and November-January; and in the three time intervals: 13-15, 16-18, and 19-21 UT, respectively. The numbers represented in black (red) above each bar in these figures indicate the number of hours (nights) over which MSTIDs were observed and the number of hours (nights) that the sky conditions were clear. Thus, the ratio of these two hourly numbers is the occurrence rate. If MSTIDs are generated by the tropospheric activity, the real occurrence rate would become higher because cloudy sky data is omitted from the analysis. The average F10.7 index in each year, which is a measure of the solar activity, is shown at the bottom of Figure 3.3(a). From Figure 3.3(a), the occurrence rate in 2004 of $\sim$46% is the highest over the 7 years observed. The occurrence rate then decreases from 2004 to 2008 with decreasing solar activity. From Figure 3.3(b), the occurrence rate in May-July of $\sim$39% is the highest of the four seasons. In the

other seasons, the rates are ∼20-30%. From Figure 3.3(c), the occurrence rate at 13-15 UT (pre-midnight) is the highest of the three time intervals. The rate then decreases from pre- to post-midnight. The time and season dependences of the occurrence rate are almost the same as those found by *Shiokawa et al.* [2006].

Figures 3.4(a)-(c) show the percentages of propagation directions of the observed MSTIDs over the total 7 years and in each year from 2003 to 2009, in the four seasons, and in the three time intervals, respectively. We categorized the propagation directions into eight sectors. Eastward- and westward-moving MSTIDs were not observed in the 630-nm images. Southward-moving MSTIDs were most frequently observed at Kototabang. Year, season, and time dependences are not clearly evident in these figures.

Figures 3.5(a)-(c) show the averages and standard deviations of the horizontal phase velocities of the observed MSTIDs in each year from 2003 to 2009, in the four seasons, and in the three time intervals, respectively. From Figure 3.5(a), the average horizontal phase velocity in 2004 is the smallest for the years observed. The velocity then increases with decreasing solar activity. Clear season and time trends are not seen in Figures 3.5(b) and 3.5(c).

Figures 3.6(a)-(c) show the averages and standard deviations of the periods of the observed MSTIDs in each year from 2003 to 2009, in the four seasons, and in the three time intervals, respectively. In all figures, MSTID periods are predominantly stable at ∼40-50 min. Note that we determined these periods using the deviations from the 1-h running averages in the images and keograms. Thus, waves with periods greater than 1 h are omitted in the analysis.

Finally, Figures 3.7(a)-(c) show the averages and standard deviations of the horizontal wavelengths of the observed MSTIDs in each year from 2003 to 2009, in the four seasons, and in the three time intervals, respectively. We calculated these wavelengths by multiplying the phase velocities by the periods. From Figure 3.7(a), the wavelength increases with decreasing solar activity. The trends in horizontal-wavelength variations are almost the same as those in horizontal phase velocity variations (Figure 3.5), because the periods are nearly constant, as mentioned above.

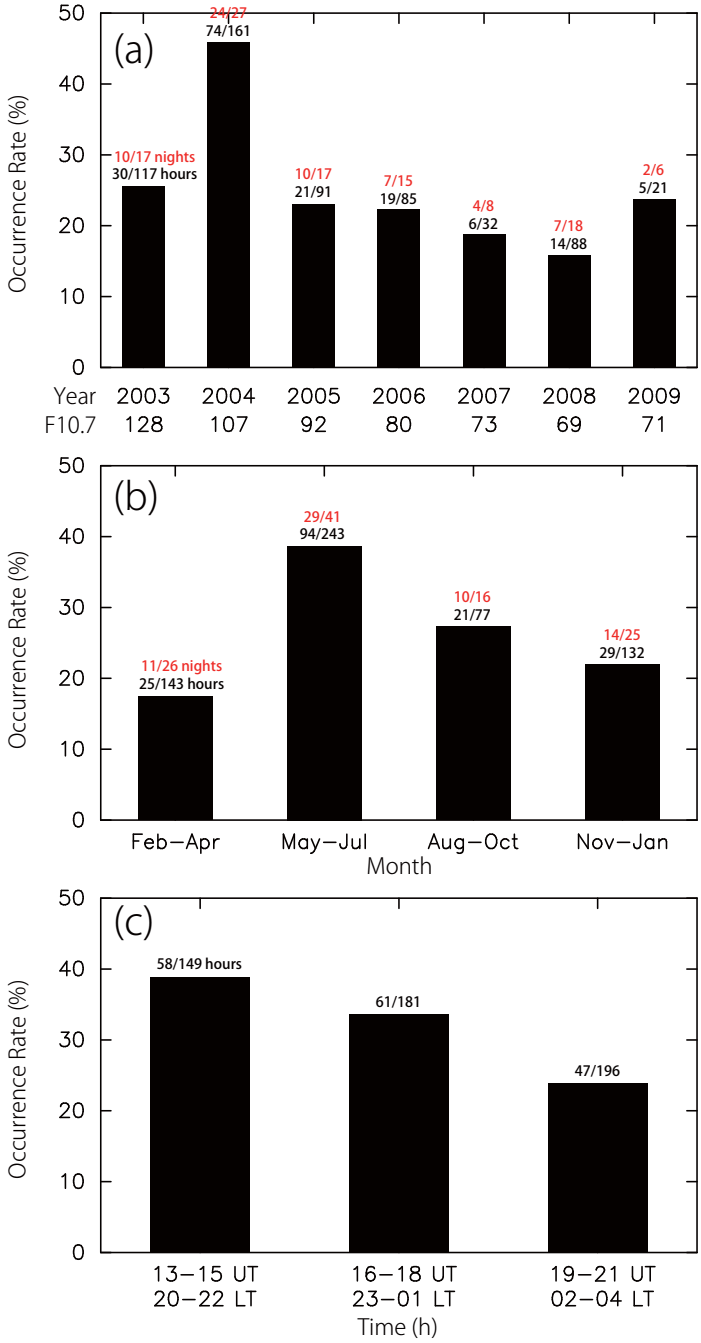

Figure 3.3: Occurrence rates of MSTIDs observed at Kototabang in (a) each year from 2003 to 2009; (b) the four seasons: February-April, May-July, August-October, and November-January; and (c) the three time intervals: 13-15, 16-18, and 19-21 UT. The numbers represented in black (red) above each bar indicate the number of hours (nights) over which MSTIDs were observed and the number of hours (nights) in which sky conditions were clear. The F10.7 index averaged over each year is shown at the bottom of (a).

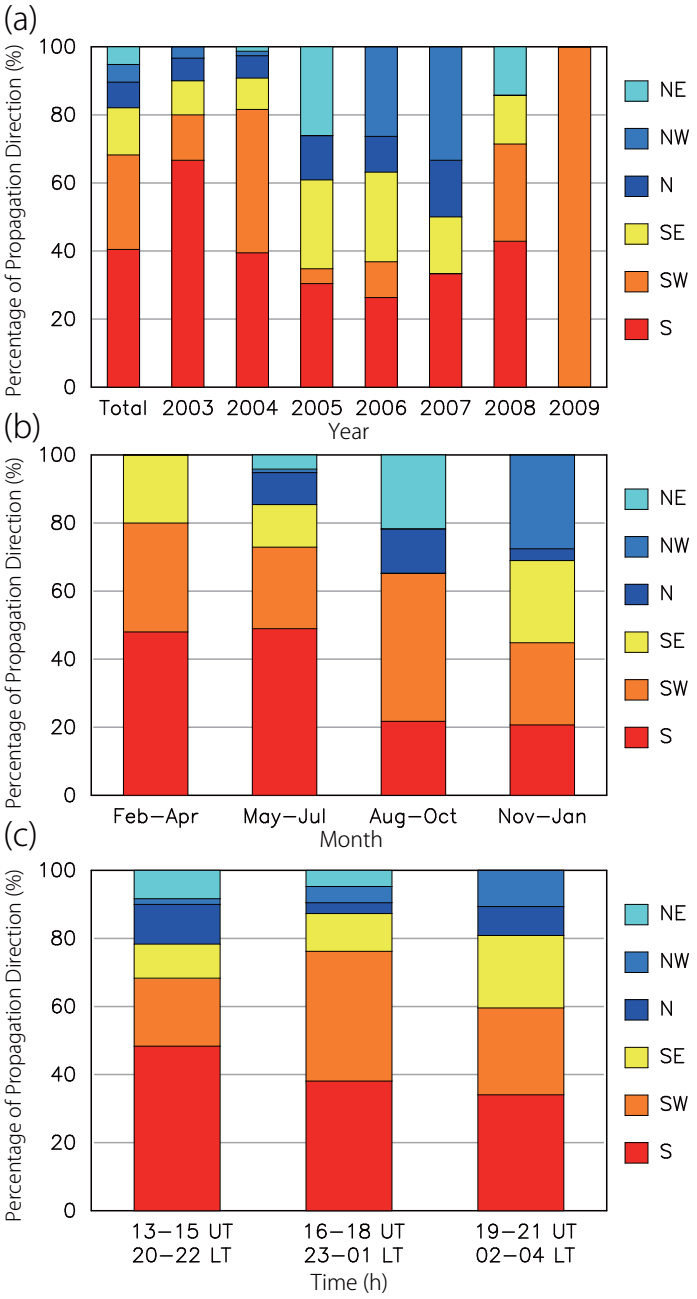

Figure 3.4: Percentages of MSTID propagating in each direction observed at Kototabang in (a) the total 7-year observation period and each year from 2003 to 2009, (b) the four seasons, and (c) the three time intervals.

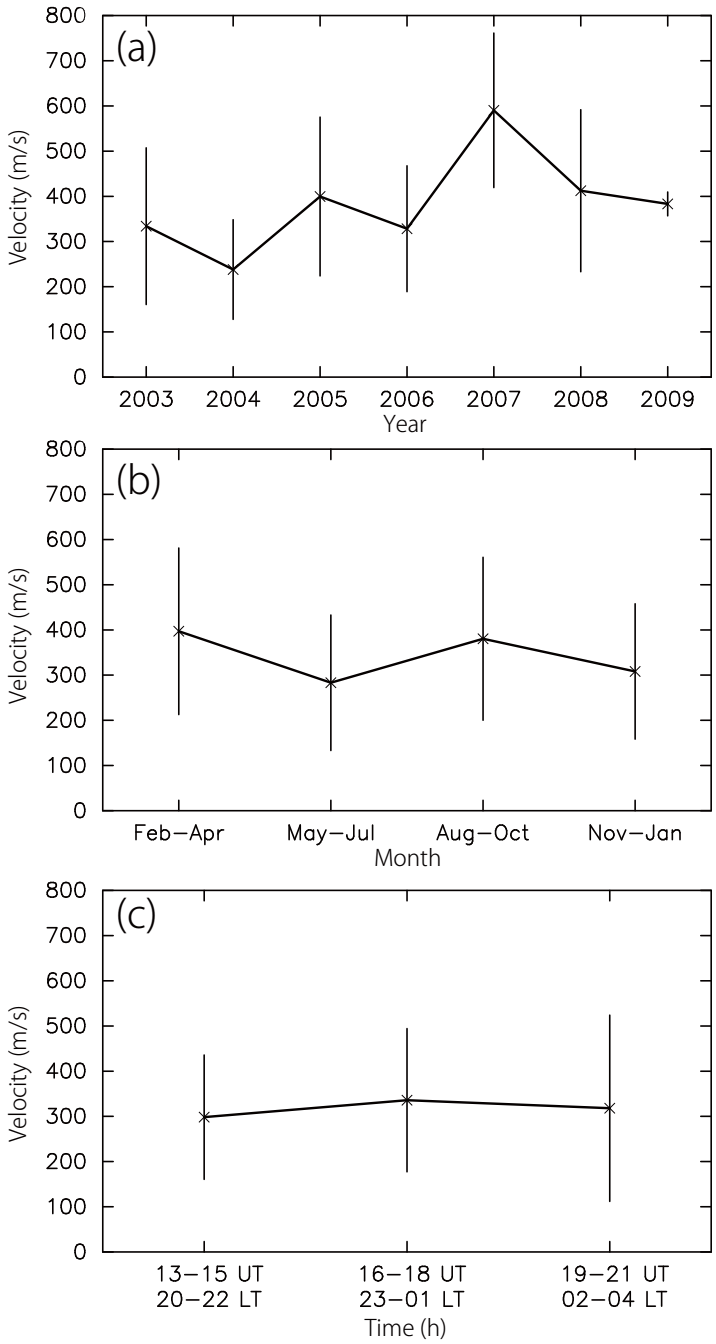

Figure 3.5: Averages and standard deviations of horizontal phase velocities of the MSTIDs observed at Kototabang in (a) each year from 2003 to 2009, (b) the four seasons, and (c) the three time intervals.

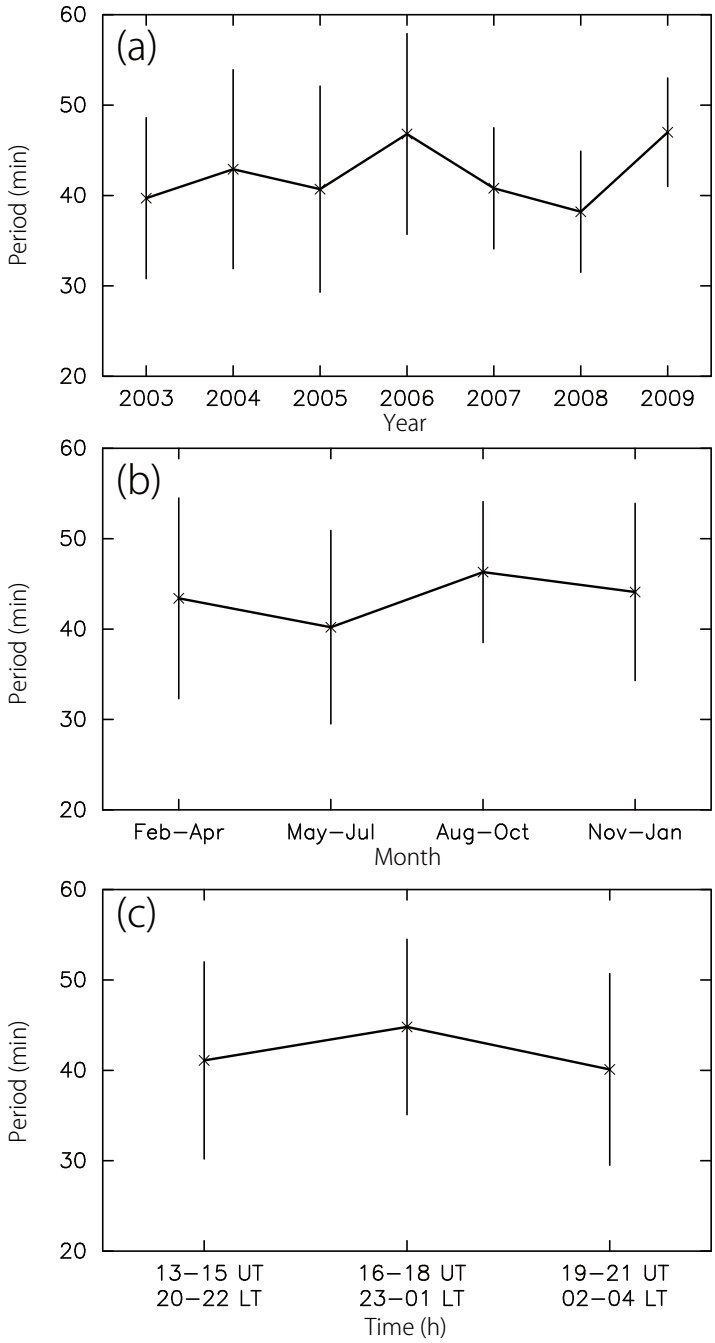

Figure 3.6: Averages and standard deviations of periods of the MSTIDs observed at Kototabang in (a) each year from 2003 to 2009, (b) the four seasons, and (c) the three time intervals.

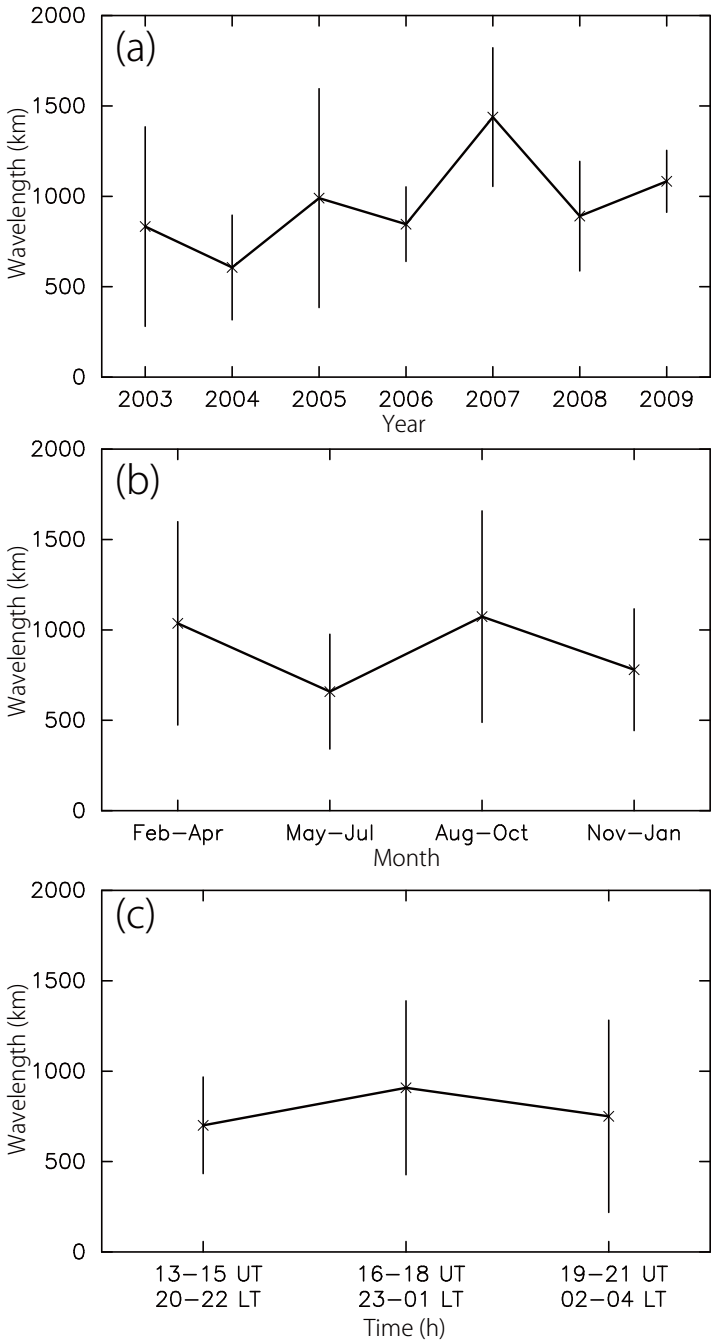

Figure 3.7: Averages and standard deviations of horizontal wavelengths of the MSTIDs observed at Kototabang in (a) each year from 2003 to 2009, (b) the four seasons, and (c) the three time intervals.

3.3 Discussion

3.3.1 Equatorial ionization anomaly

We observed MSTIDs in the 630-nm airglow images at Kototabang, Indonesia during a 7-year period from October 2002 to October 2009. MSTIDs were frequently observed in the high-intensity airglow region, which corresponds to the equatorial ionization anomaly. The anomaly is generated by the ionospheric fountain effect [*Fejer et al.*, 1991]. At equatorial latitudes, the ionospheric electric field is directed eastward during the daytime. This eastward electric field generates upward $\mathbf{E} \times \mathbf{B}$ drift. As a result, high-density plasma is usually located between 10° and 20° north and south of the geomagnetic equator due to gravity diffusion. After the sunset terminator, the electric field turns to be directed westward [*Fejer et al.*, 1991]. The anomaly moves toward the geomagnetic equator due to equatorward/downward $\mathbf{E} \times \mathbf{B}$ drift. The northward motion of the anomaly seen in Figure 3.1(a) is considered to correspond to this equatorward motion. The altitude of the 630-nm airglow layer in the anomaly region would be lower than that at the equator side of the anomaly, because ionospheric plasma located in the equator side of the anomaly is lifted up due to the fountain effect. This may explain why MSTIDs were observed in the anomaly, since gravity waves dissipate in the thermosphere due to molecular viscosity, and therefore might not be able to survive to the higher altitudes on the equator side of the anomaly [*Vadas*, 2007].

3.3.2 Discussion of 7-year statistics

The propagation directions of MSTIDs observed at Kototabang were predominantly southward, as shown in Figure 3.4. In contrast, nighttime MSTIDs typically observed at middle latitudes in the northern hemisphere have been found to propagate southwestward. The horizontal scale of such middle-latitude MSTIDs was ∼100-500 km [e.g., *Saito et al.*, 2001; *Shiokawa et al.*, 2003; *Kotake et al.*, 2007], which is smaller than that of MSTIDs at Kototabang. These differences between nighttime MSTIDs at middle and equatorial latitudes suggest that they are caused by different sources. In the southern hemisphere, MSTIDs with phase fronts elongated in a northwest-southeast direction cannot be explained through the Perkins instability [*Perkins*, 1973]. Southward MSTIDs with phase fronts elongated in an east-west direction are possibly caused by gravity waves, because neutral oscillation resulting from gravity waves moves plasma meridionally along the geomagnetic field line.

The occurrence rate of the observed MSTIDs was highest in 2004 and decreased with decreasing solar activity. This fact suggests two possibilities. One possible cause of the decrease is that the gravity waves, which are one of the sources of MSTIDs, could dissipate in the thermosphere at lower altitudes during low solar activity than during high solar activity. This low-altitude dissipation is due to the neutral viscosities which increase with decreasing neutral density [*Vadas and Fritts*, 2005; *Vadas*, 2007]. The neutral density decreases with decreasing solar activity. The second possibility is that the signal-to-noise ratio of the airglow intensity decreased because the airglow emissions become weaker during periods of low solar activity. We should note that the sensitivity of the imager declined during later measurements at the solar minimum, which may also have caused the decrease in MSTID occurrence. However, the effect on decrease of MSTID occurrence by the sensitivity degradation would be minor, since we took the deviation against the background airglow intensity, as shown in equation (3.1). We should also note that the occurrence rate was highest in 2004 while the average F10.7 index decreases from 2003 to 2008, as shown in Figure 3.3(a). This fact that the smaller occurrence in 2003 compared with the occurrence in 2004 probably results from the imager stop during June-August 2003, because the MSTIDs

were frequently observed in May-July, as shown in Figure 3.3(b).

Vadas [2007] found, from a simulation of gravity wave propagation in the thermosphere, that gravity waves with small horizontal wavelengths cannot propagate to higher altitudes in the thermosphere. Dissipation altitudes are lower (higher) for gravity waves with smaller (larger) horizontal wavelengths for the same fixed period, as shown in Figures 4 and 6 of Vadas' report. Her simulation also revealed that gravity waves cannot propagate to higher altitudes when the thermospheric temperature is low. For gravity waves with a horizontal wavelength of ∼800 km and a period of ∼40 min, the simulated dissipation altitudes were ∼200, 240, 260, and 275 km under thermospheric temperature conditions of $T = 600$ (solar minimum), 1000, 1500, and 2000 K (solar maximum), respectively. This result infers that gravity waves of ∼800-km horizontal wavelength dissipate at the bottom of the F region during the solar minimum. Hence, only the gravity waves with larger horizontal wavelength would propagate into the thermosphere during the solar minimum. Therefore, the average horizontal wavelength becomes larger with decreasing solar activity, which is consistent with our observation as shown in Figure 3.7(a). Our observation suggests that the observed MSTIDs are caused by gravity waves in the thermosphere.

From Figures 3.3(a), 3.3(b), 3.7(a) and 3.7(b), the average horizontal wavelength is relatively small when the occurrence rate is high (in 2004 and in May-July). From Vadas' simulation, MSTIDs having large horizontal wavelengths and relatively small periods easily propagate into the thermosphere. Our observations appear to indicate that MSTIDs with both small and large horizontal wavelengths are observed when the occurrence rate is high. As a result, the average horizontal wavelength would become relatively small. Conversely, we speculate that MSTIDs with small horizontal wavelengths dissipate in the thermosphere when the occurrence rate is low. In such case, the average horizontal wavelength would become larger.

The simulated result by *Vadas* [2007], however, showed that the solution of gravity waves with a horizontal wavelength of ∼800 km and an intrinsic period of ∼40 min does not exist in the lower atmosphere at altitudes below 80 km. The typical horizontal phase velocity, v_{ph}, of observed MSTIDs was ∼330 m/s (=800 km/40 min). In the lower atmosphere, gravity waves with an intrinsic

phase speed larger than the sound speed (∼300 m/s) cannot exist. The source of such waves may be located in the thermosphere.

One may argue that the winds in the lower atmosphere allow the intrinsic phase speed to be smaller than the sound speed even for the waves with $v_{ph} \simeq 330$ m/s in the thermosphere. However, because tides are a major contributor to the winds in the lower atmosphere, and because the vertical wavelengths of the tides are less than 50 km, the signs of the neutral horizontal winds typically change several times in the lower atmosphere. Although the ∼330 m/s waves might survive in a 20-30 km portion of the lower atmosphere, it could not propagate the entire way up from the troposphere to the thermosphere. Therefore, the observed MSTIDs with $v_{ph} \geq 300$ m/s, which are 46% (33 events) of the observed total MSTID events (71 events), would be caused by secondary gravity waves generated in the thermosphere. The thermospheric source of the secondary gravity waves may be the body force caused by dissipation of the primary gravity waves propagating from the lower atmosphere. However, the observed MSTIDs with $v_{ph} \leq 300$ m/s, which are 54% (38 events) of the total events, can be caused by the primary gravity waves which possibly propagate from the lower atmosphere into the thermosphere.

3.3.3 Comparison between propagation direction and tropospheric convection

If MSTIDs are caused by the primary gravity waves generated from the troposphere, strong tropospheric convection activity must be located in the source direction of MSTIDs [e.g., *Röttger*, 1977]. Since the gravity waves propagate away from the source region, we can infer the source location from the observed propagation directions. However, this consideration is not applicable for the case that the intrinsic phase speed is larger than the sound speed in the lower atmosphere. In this study, we compared the observed propagation directions of MSTIDs with the locations of tropospheric convection activity as identified by equivalent black body temperature (Tbb) for MSTIDs with $v_{ph} \leq 300$ m/s. Under this condition, 38 MSTID events out of 71 events were available. Here, Tbb indicates the cloud-top temperature observed by geostationary satellites. Low (high) Tbb indicates

strong (weak) tropospheric convection [e.g., *Tsuda and Hocke*, 2004].

Figures 3.8(a) and 3.8(b) show maps of Tbb measured on 9 May 2004 and 14 December 2004, respectively. These maps are constructed by averaging the hourly Tbb over Δt ($= \Delta t_0 - 2$ h), where Δt_0 is the time interval over which MSTIDs were observed, because it would take a few hours for gravity waves to propagate from the troposphere to the thermosphere. The propagation direction of MSTIDs observed on 9 May 2004 was south-southeastward (13° eastward from south). The horizontal phase velocity, period, and horizontal wavelength are ∼200 m/s, ∼35 min, and ∼420 km, respectively. If these MSTIDs were propagating directly from the troposphere to the thermosphere, the source region of MSTIDs must be to the north-northwest of Kototabang. An area of strong convection, where Tbb values are ∼200-230 K, is located between latitudes of 10°N and 15°N and between longitudes of 70°E and 105°E, as shown in Figure 3.8(a). In this case, MSTIDs are possibly caused by the gravity waves generated from this tropospheric convection activity, because the propagation direction of MSTIDs is consistent with the location of the tropospheric convection. Conversely, the propagation direction of MSTIDs observed on 14 December 2004 was south-southwestward (29° westward from south). The horizontal phase velocity, period, and horizontal wavelength are ∼200 m/s, ∼40 min, and ∼480 km, respectively. Thus, the source region of the MSTIDs is expected to be to the north-northeast of Kototabang. However, the majority of Tbb values in this direction are high (∼280-300 K), as shown in Figure 3.8(b), indicating that strong convection does not exist for this event in the expected source direction.

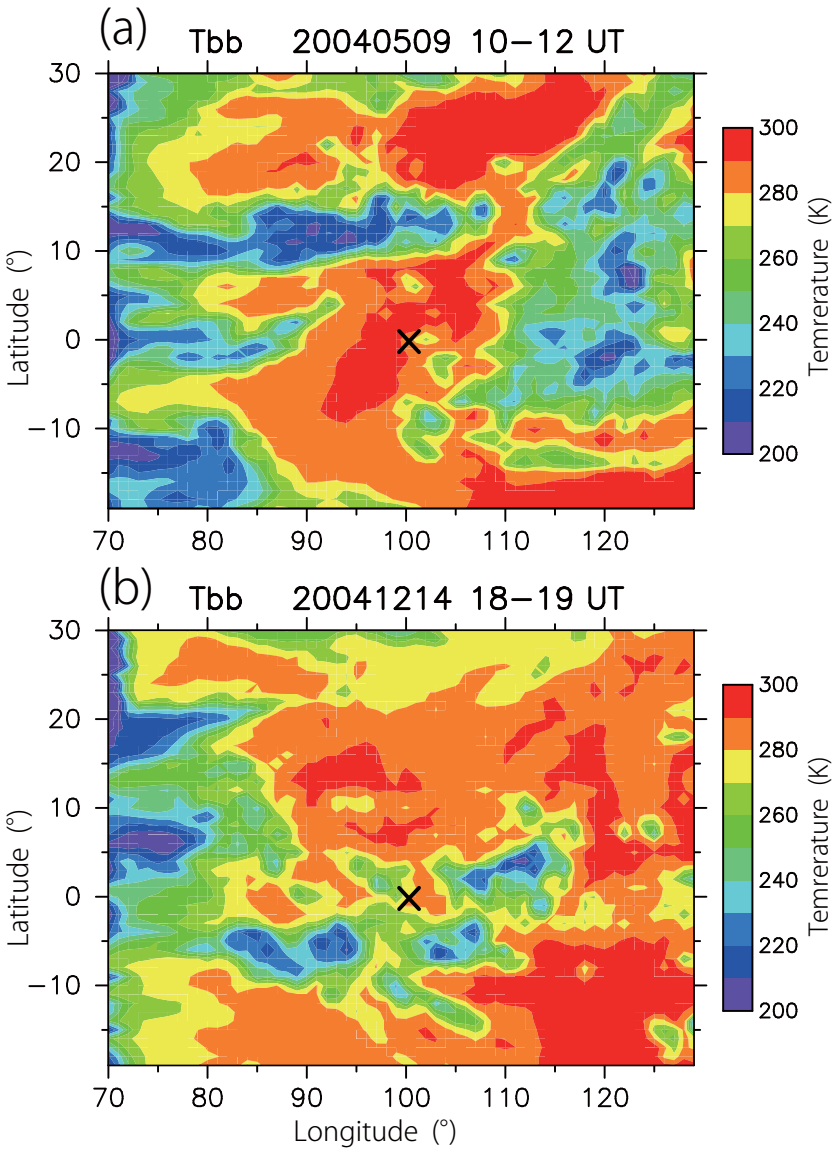

Figure 3.8: Tbb maps on (a) 9 May 2004 from 10 to 12 UT and (b) 14 December 2004 from 18 to 19 UT. These maps are constructed by averaging the hourly Tbb over Δt ($= \Delta t_0 - 2$ h), where Δt_0 is the time interval over which MSTIDs were observed. X denotes the location of Kototabang in each figure. Low Tbb indicates strong tropospheric convection in these maps.

By using these Tbb maps in combination with the observed MSTID propagation directions, we classified MSTID events, for $v_{ph} \leq 300$ m/s, into three categories: 1) strong convection exists within ±10 degrees from the source direction which is determined by the observed MSTID propagation direction, 2) strong convection exists within ±10-30 degrees from the source direction, and 3) strong convection does not exist within ±30 degrees from source direction. These criteria were chosen by considering that the variation of the horizontal background wind may allow ±30 degree variation of propagation direction of gravity waves from the troposphere to the thermosphere. We consider that strong convection corresponds to Tbb values of less than 230 K. From these criteria, 55% (=21/38 events) of the MSTID events correspond to the case 1), 26% (=10/38 events) to the case 2), and 19% (=7/38 events) to the case 3) during the 7-year observation period. Therefore, we suggest that 81% (=55%+26%) of MSTIDs with $v_{ph} \leq 300$ m/s are caused by primary gravity waves which have originated from strong convection in the troposphere, and then they propagated directly from the troposphere to the thermosphere.

A similar comparison with tropospheric convection activity by using Tbb was carried out by *Ogawa et al.* [2009]. They found that GPS scintillation over Kototabang caused by plasma bubbles was correlated to tropospheric disturbances located to the west of Kototabang identified by Tbb. Their results indicated that atmospheric waves generated from the troposphere, such as gravity waves and planetary waves, contribute to the ionospheric disturbances. However, we must also consider other MSTID sources, because strong tropospheric convection in the expected source direction does not exist in 19% of the MSTID events for $v_{ph} \leq 300$ m/s. One possible source of MSTIDs is secondary gravity waves generated in the thermosphere by dissipation of primary gravity waves originating from the lower atmosphere. The horizontal wavelengths of secondary gravity waves in the thermosphere would be ∼100-2000 km [*Vadas and Crowley*, 2010], which can explain the horizontal wavelengths of the observed MSTIDs. The other possible sources are gravity waves generated by upper-tropospheric jet streak [e.g., *Zhang*, 2004].

Figures 3.9(a)-(e) show average Tbb maps for the total 7 years, February-April, May-July, August-October, and November-January, respectively. These

maps are constructed by averaging the hourly Tbb over Δt ($= \Delta t_0 - 2$ h), where Δt_0 is the time interval over which MSTIDs were observed in each period. The distribution of tropospheric convection over the total 7-year period in Figure 3.9(a), is similar to that for May-July in Figure 3.9(c), because MSTIDs were most frequently observed in this season. From these figures, tropospheric convection activity is not seen to the south of Kototabang in all seasons, implying that northward-moving gravity waves should not be frequently observed at Kototabang. From Figures 3.9(c) and 3.9(d), the tropospheric convection activity characterized by low Tbb is seen to the north of Kototabang in May-July and August-October. These convection zones correspond to the intertropical convergence zone (ITCZ) in which strong convection exists. The occurrence rate of the observed MSTIDs is the highest in May-July, as shown in Figure 3.3(b). The gravity waves generated in ITCZ are thought to propagate to Kototabang to produce the southward-moving MSTIDs. In February-April and November-January, tropospheric convection activity is located over Kototabang, as shown in Figures 3.9(b) and 3.9(e), respectively. In these seasons, gravity waves with periods of $\sim$40 min may not be observed in the thermosphere over Kototabang, because gravity waves generated from the tropospheric convection at Kototabang could propagate into the thermosphere at a point outside of the field-of-view of the airglow imager at Kototabang due to larger horizontal wavelengths than vertical wavelengths.

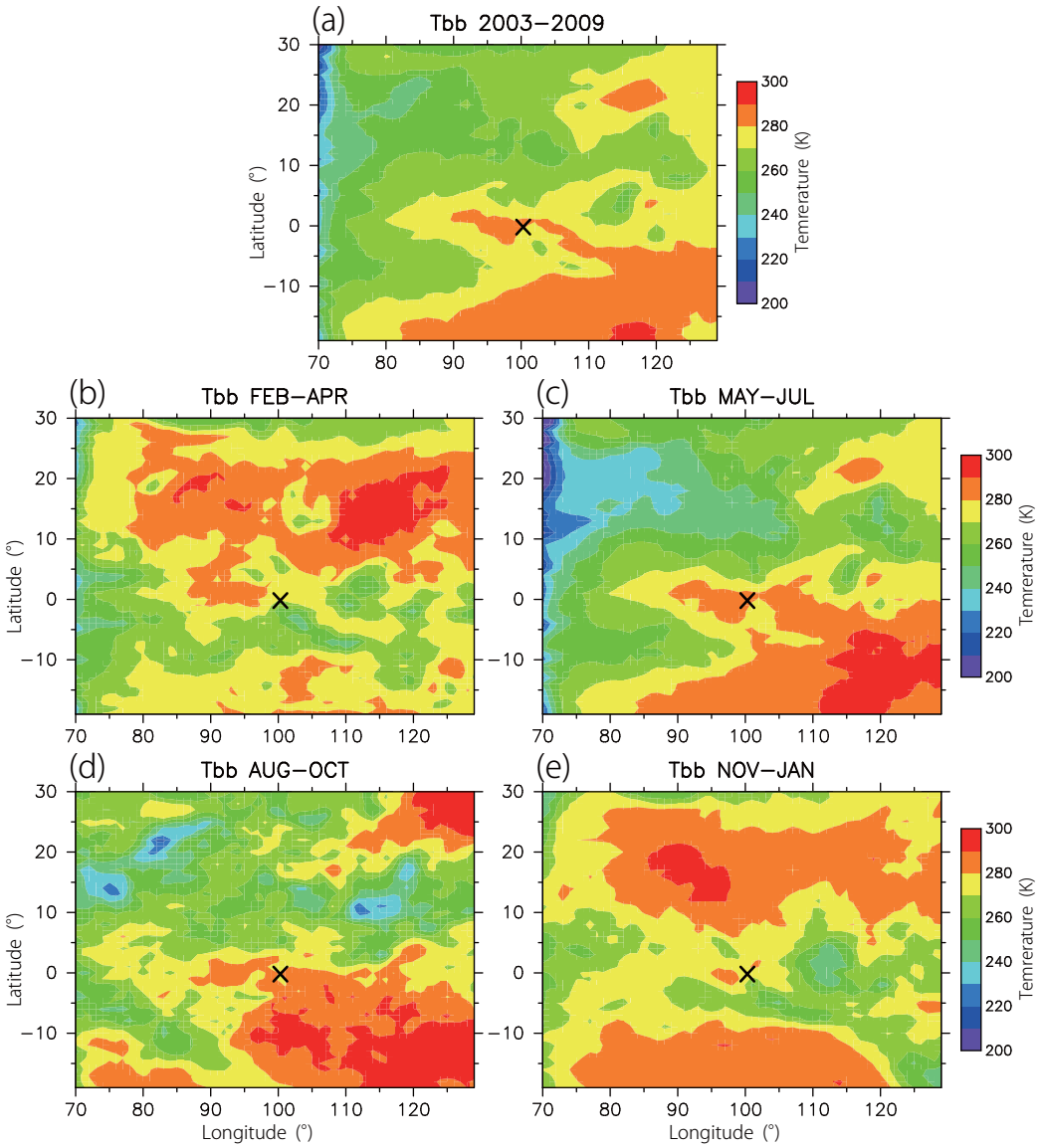

Figure 3.9: Average Tbb maps for (a) the total 7 years, (b) February-April, (c) May-July, (d) August-October, and (e) November-January. These maps are constructed by averaging the hourly Tbb over Δt ($= \Delta t_0 - 2$ h), where Δt_0 is the time interval over which MSTIDs were observed in each period. X denotes the location of Kototabang in each figure.

3.3.4 Dispersion relation for gravity waves

If gravity waves are the MSTID source, then MSTIDs must satisfy the following linear dispersion relation for the gravity waves [*Hines*, 1960];

$$m^2 = \frac{N^2}{(u-c)^2} - k^2 - \frac{1}{4H^2}, \tag{3.2}$$

where m ($= 2\pi/\lambda_z$), N, u, c, k ($= 2\pi/\lambda_h$), and H are the vertical wavenumber, Brunt-Väisälä frequency, background neutral wind velocity, horizontal phase velocity of the waves, horizontal wavenumber, and density scale height, respectively. Gravity waves dissipate at an altitude where $\mid u - c \mid = 0$. This process is called the filtering effect by the background neutral wind. For typical MSTIDs with a horizontal phase velocity of ∼330 m/s, $\mid u - c \mid$ does not become to be zero because the neutral wind velocity, u, in the thermosphere is usually less than 200 m/s [e.g., *Biondi et al.*, 1991; *Brum et al.*, 2012].

The Brunt-Väisälä frequency is 8-11 $\times 10^{-3}$ rad/s and the scale height is 30-50 km at altitudes of 200-300 km in the thermosphere. By neglecting the small k^2 term in equation (3.2), the $m^2 > 0$ propagating condition of gravity waves gives $\mid u - c \mid < 2NH$. This condition indicates that gravity waves with an intrinsic phase speed larger than the sound speed cannot propagate in the atmosphere [e.g., *Hines*, 1960]. The value of $2NH$ is ∼500-1000 m/s in the thermosphere. Thus, MSTIDs with a horizontal phase velocity of ∼330 m/s satisfy the above dispersion relation for the gravity waves. However, below the mesopause region, the value of $2NH$ is smaller than 300 m/s. Thus, MSTIDs may not satisfy the dispersion relation for the gravity waves propagating in the lower atmosphere, depending on the background neutral wind velocity. In such cases, secondary waves generated in the thermosphere by dissipation of the primary gravity waves from the lower atmosphere may be the direct cause of the observed MSTIDs [e.g., *Vadas and Crowley*, 2010].

3.4 Conclusions

We have observed nighttime MSTIDs by using an all-sky imager at Kototabang, Indonesia. MSTIDs were observed in 630-nm nighttime airglow images. We statistically analyzed MSTIDs observed over a 7-year period from 26 October 2002 to 25 October 2009. The occurrence rate of the observed MSTIDs decreased with decreasing solar activity. The average horizontal wavelength increased with decreasing solar activity. Southward-moving MSTIDs were dominant throughout the 7 years. Our results are consistent with the hypothesis that the observed MSTIDs are caused by gravity waves in the thermosphere. The 46% of the observed MSTIDs would be caused by the secondary gravity waves generated in the thermosphere, since their phase speeds, v_{ph}, are larger than the sound speed ($\sim$300 m/s) in the lower atmosphere. We also compared the propagation directions of the observed MSTIDs with the locations of the tropospheric convection activity identified by Tbb. We applied this comparison to the MSTID events for $v_{ph} \leq 300$ m/s which could exist as gravity waves in the lower atmosphere. In 81% of MSTID events for $v_{ph} \leq 300$ m/s (44% of the total events), we found strong tropospheric convection in the source direction inferred by the direction of the observed MSTID propagation. We suggest that primary gravity waves generated from strong convection in the troposphere produce the observed MSTIDs for these cases.

Chapter 4

Geomagnetically conjugate observation of plasma bubbles and thermospheric neutral winds at low latitudes

Chapter 3 described MSTIDs observed in the low-latitude ionosphere. We suggested that gravity waves generated in the lower atmosphere propagate into the thermosphere, and are observed as MSTIDs in the 630-nm airglow images. On the other hand, electric fields would also play an important role in the dynamics of the equatorial ionosphere. The F-region dynamo effect generates the ionospheric electric field as neutral winds blow across geomagnetic field lines [e.g., *Rishbeth*, 1971]. At equatorial latitudes, the electric field has been measured by incoherent scatter radars through $\mathbf{E} \times \mathbf{B}$ drift [e.g., *Fejer et al.*, 1985]. The electric field can be also estimated by using the drift velocity of plasma bubbles observed in 630-nm airglow images [e.g., *Sobral et al.*, 2009]. When the bubble growth ends after post sunset hours, plasma bubbles keep a constant shape for several hours. Thus, we can assume that the plasma bubbles propagate at the speed close to the background ion drift, which is taken as $\mathbf{E} \times \mathbf{B}$ drift.

To investigate the F-region dynamo process, the electric field and neutral winds must be measured simultaneously. *Chapagain et al.* [2012; 2013] compared the

drift velocity of the plasma bubbles with the velocity of neutral winds observed by FPIs at equatorial latitudes. However, neutral winds were observed in only the southern hemisphere in their studies. Since the electric field is generated by neutral winds in both hemispheres, we should simultaneously observe the drift velocity of plasma bubbles and the velocity of neutral winds in both hemispheres.

In Chapter 4, we report simultaneous observation of plasma bubbles and the thermospheric neutral winds at Kototabang, Indonesia, and Chiang Mai, Thailand, which are located nearly geomagnetically conjugate points. Such conjugate observations of plasma bubbles combined with the thermospheric winds are being realized for the first time. We compared the eastward drift velocities of the observed plasma bubbles with those estimated from the observed neutral winds and modeled conductivity. The study in Chapter 4 has been reported by *Fukushima et al.* [2015].

4.1 Observations

Figure 2.1 shows the locations of Kototabang and Chiang Mai and the locations of their geomagnetic conjugate points. The conjugate points are calculated from the 11th generation of the International Geomagnetic Reference Field (IGRF-11) [*Finlay et al.*, 2010] by tracing geomagnetic field lines. Black circles show the field-of-view of each airglow imager. Chiang Mai is roughly the conjugate point of Kototabang; the exactly conjugate point of Kototabang (GLAT: 15.9°N) is just ∼3° south of Chiang Mai, as seen in the figure. Thus, airglow observations at low-latitude geomagnetically conjugate points became available after we installed the imager at Chiang Mai.

Plasma bubbles were observed in the 630-nm airglow images for 7 hours, from 13 to 20 UT (from 20 to 03 LT) on 5 April 2011, simultaneously at Kototabang, Indonesia (GLON: 100.3°E, GLAT: 0.2°S, MLAT: 10.0°S), and Chiang Mai, Thailand (GLON: 98.9°E, GLAT: 18.8°N, MLAT: 8.9°N). The MLATs of Kototabang and Chiang Mai are calculated by the IGRF model. Note that the MLAT of Kototabang in 2011 changed ∼0.6° from that described in Chapter 3.

Figures 4.1(a) and 4.1(b) show the 630-nm all-sky image taken at 1523 UT by the all-sky airglow imager at Kototabang and the image taken at 1522 UT by the

imager at Chiang Mai, respectively. The plasma bubbles are seen in the images as meridionally aligned depletions in the 630-nm airglow intensity at Kototabang and Chiang Mai. The sky at Chiang Mai was rather cloudy on the observation night. Despite this, bubbles are discernible in the image. Inside the bubbles, 630-nm airglow intensity was extremely low, indicating that the F-region plasma density inside the bubbles was much lower than that outside the bubbles on 5 April 2011.

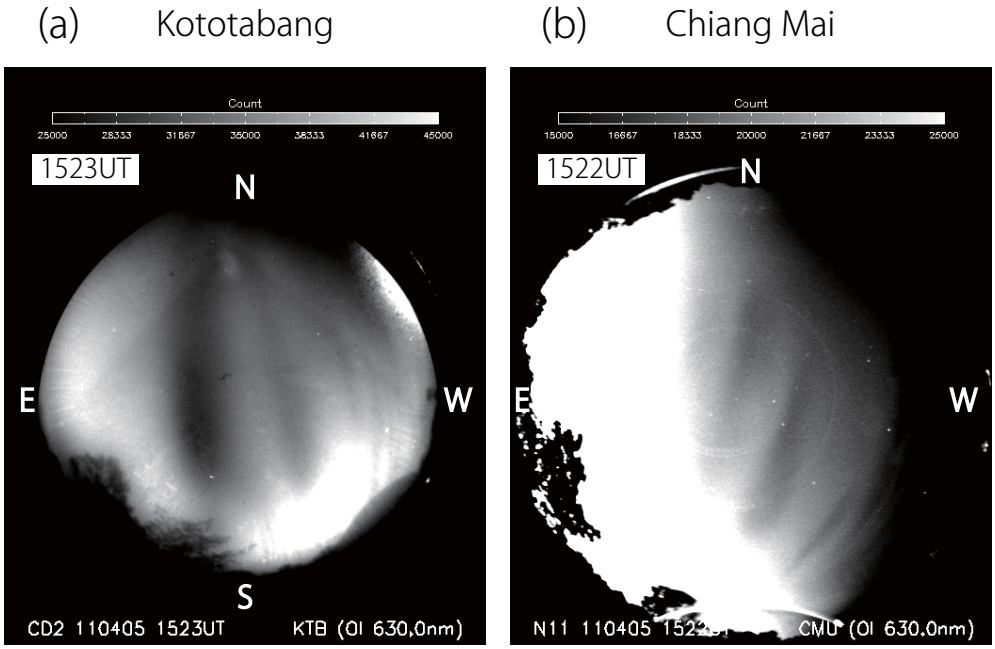

Figure 4.1: All-sky images simultaneously obtained by two airglow imagers at (a) Kototabang and (b) Chiang Mai on the night of 5 April 2011. Up is geographic north and left is geographic east.

Figures 4.2(a)-(d) and 4.2(e)-(h) show the 630-nm images of Chiang Mai from 1458 to 1610 UT and Kototabang from 1458 to 1612 UT, respectively. These images are converted into geographic coordinates and represented as deviations $\Delta I(t)$ from 1-h running averages $I_a(t)$ as equation (3.1). Note that the amplitudes of bubbles in percentages are considerably different between the two stations. This is because we defined the deviations $\Delta I(t)$ by using raw CCD counts as $I(t)$ in Figures 4.2(a)-(d) at Chiang Mai and by using absolute airglow intensity as $I(t)$ in Figures 4.2(e)-(h) at Kototabang. Strong urban light pollution prevented us from calculating the absolute intensity for the Chiang Mai data, though continuum light pollution does not affect Doppler wind measurement by FPI. Declination angles at an altitude of 250 km over Kototabang and Chiang Mai are -0.55 and -0.91 degrees, respectively. Thus, magnetic and geographic east are almost the same. Plasma bubbles are clearly seen in the images; these are represented in black in Figures 4.2(a)-(d) and in blue in Figures 4.2(e)-(h). The bubbles moved eastward at both Chiang Mai and Kototabang.

To see the conjugacy of the plasma bubbles, we projected the images of Kototabang onto the conjugate point of Kototabang in the northern hemisphere (GLON: 100.1°E; and GLAT: 15.9°N). We then combined the projected images of Kototabang (bottom half in Figures 4.2(i)-(l)) with the images of Chiang Mai (top half in Figures 4.2(i)-(l)). The bubble structures that were observed at Kototabang and Chiang Mai fit very well. This result is consistent with plasma bubbles observed at middle-latitude conjugate points [e.g., *Otsuka et al.*, 2002], indicating that the bubbles observed at low latitudes also develop along geomagnetic field lines.

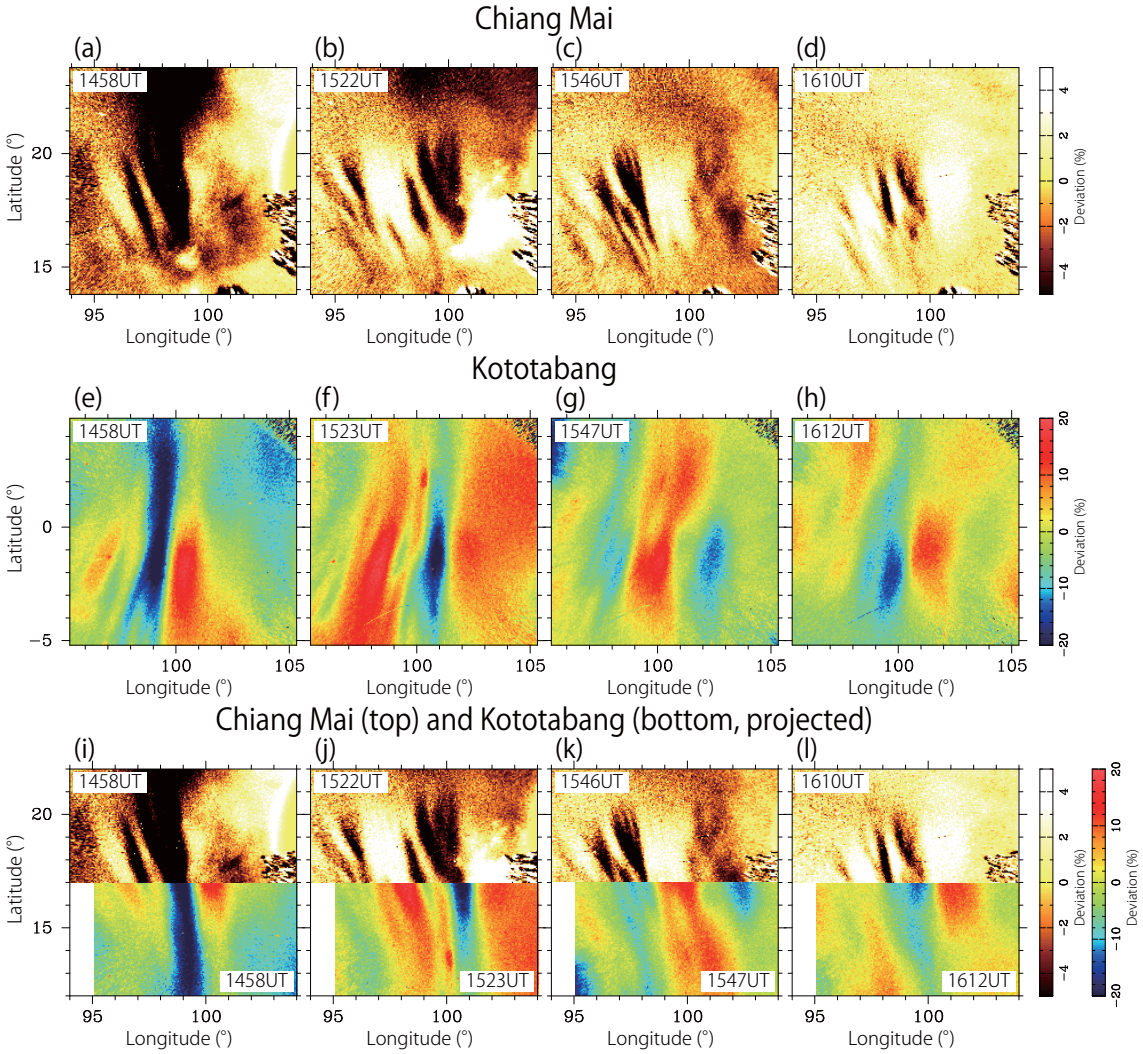

Figure 4.2: Two-dimensional images of the 630-nm airglow represented as deviations $\Delta I(t)$ from 1-h running averages $I_a(t)$. (a)-(d) Images at Chiang Mai from 1458 to 1610 UT. (e)-(h) Images at Kototabang from 1458 to 1612 UT. These images are converted to geographic coordinates. Deviations are defined by using raw CCD counts in (a)-(d) and by using absolute airglow intensity in (e)-(h). (i)-(l) The top and bottom half of each panel is the image at Chiang Mai and the projected image of Kototabang, respectively. The bottom half images of (i)-(l) are projected onto the northern hemisphere along the geomagnetic field line.

Figures 4.3(a) and 4.3(b) show variation in the 630-nm airglow intensity from 13 to 22 UT (from 20 to 05 LT) for a zonal keogram over Chiang Mai images at the latitude of Chiang Mai (18.8°N) and a zonal keogram over Kototabang images at the latitude of the conjugate point of Chiang Mai (3.0°S), respectively. These keograms are converted into geographic coordinates and represented as deviations from 1-h running averages of data in Figure 4.2. In both keograms, eastward-moving plasma bubbles were seen from 13 to 20 UT (from 20 to 03 LT) at periods of ∼50-80 min. The bubbles were observed at 1510, 1610, and 1920 UT at Chiang Mai (at a longitude of 98.9°E, shown in Figure 4.3(a)), and at 1340, 1510, 1610, 1730, 1820, and 1920 UT at the conjugate point of Chiang Mai (at a longitude of 99.2°E, shown in Figure 4.3(b)). Figure 4.3(a) shows that no bubbles were observed before 1440 UT, between 1650 and 1850 UT, and after 1940 UT; this is because the sky at Chiang Mai was cloudy at those times. The eastward drift velocities at 1340, 1510, 1610, 1730, 1820, and 1920 UT were almost the same at two conjugate points at 124, 124, 120, 116, 112, and 103 m/s, respectively. These velocities are calculated from the distances of bubble motion per time using these zonal keograms. The uncertainty of this velocity estimation due to the ambiguity of the distances per time on the keograms was ∼4 m/s. However, the difference of the drift velocities between Kototabang and Chiang Mai was within 1 m/s, indicating that accuracy of the estimated drift velocities is high. The drift velocities decreased as time passed.

Figures 4.3(c) and 4.3(d) show eastward and northward neutral wind velocities, respectively, observed by the FPIs at Kototabang and Chiang Mai. Note that the wind velocities observed at Chiang Mai were ambiguous before 1440 UT, between 1730 and 1830 UT, and after 2000 UT because the sky was cloudy. Scattering of airglow emission by clouds prevents line-of-sight Doppler shift measurement of the emission. Zonal winds observed at both stations were eastward and decreased from 15 to 18 UT (from 22 to 01 LT), as shown in Figure 4.3(c). This local-time variation in the zonal winds was similar to variation in the drift velocities of the plasma bubbles. The eastward velocities were ∼70-130 m/s at Kototabang and ∼50-90 m/s at Chiang Mai. Thus, eastward wind velocities at Kototabang were ∼20-40 m/s larger than those at Chiang Mai. On the other hand, meridional winds observed at both stations were very weak. The meridional winds at Ko-

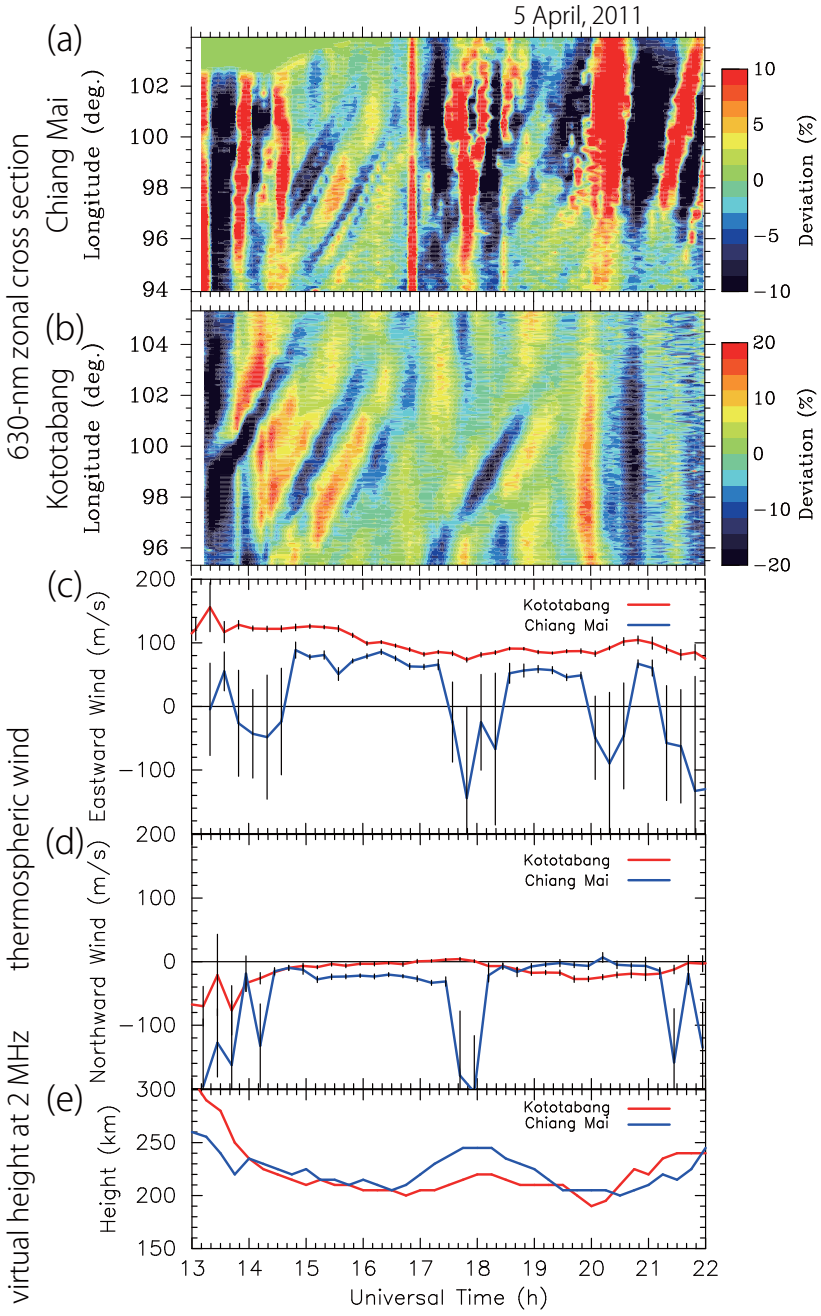

Figure 4.3: The 630-nm zonal keograms represented as deviations $\Delta I(t)$ from 1-h running averages $I_a(t)$ (a) at Chiang Mai and (b) at a latitude of 3.0°S (2.8° south of Kototabang, which is the conjugate point of Chiang Mai). Deviations are defined by using raw CCD counts in (a) and by using absolute airglow intensity in (b). Averages and standard deviations of (c) eastward and (d) northward neutral wind velocities observed by FPIs at Kototabang (red lines) and Chiang Mai (blue lines). (e) Virtual heights ($h'F$) at a frequency of 2 MHz, observed by ionosondes at Kototabang (red line) and Chiang Mai (blue line).

totabang and Chiang Mai were slightly southward after ∼18 UT and before ∼18 UT, respectively, as shown in Figure 4.3(d).

Figure 4.3(e) shows the ionospheric virtual heights ($h'F$) at a frequency of 2 MHz (corresponding to the plasma density of $\sim 5.0 \times 10^{10}$ m^{-3}), as observed by the ionosondes at Kototabang and Chiang Mai. The displayed values were taken from the ionograms. The $h'F$ at a frequency of 2 MHz corresponds to the height of the bottom-side F region. The heights over Chiang Mai were ∼20-30 km higher than those over Kototabang, especially from 17 to 19 UT. At other time intervals, the ionospheric heights were similar at the two stations. The F2-region critical frequency (f_oF_2) could not be measured because trace lines in the ionograms were spread out due to the bubble appearance, as shown in the ionogram of Figure 2.3(a).

4.2 Discussion

4.2.1 Summary of the conjugate observations

We simultaneously observed plasma bubbles at Kototabang and Chiang Mai, which were seen in 630-nm airglow images obtained by all-sky airglow imagers. The plasma bubbles continuously moved eastward from 1340 to 1940 UT with velocities of ∼100-125 m/s and periods of ∼50-90 min. The drift velocities of plasma bubbles decreased as time passed. We also simultaneously observed the thermospheric winds by using the co-located FPIs at both stations. The zonal and meridional winds, respectively, were eastward and slightly southward at Kototabang and Chiang Mai. The eastward wind velocities at Kototabang were ∼20-40 m/s larger than those at Chiang Mai. The eastward winds observed at the two stations decreased in strength from 15 to 18 UT, which was similar to the variation of plasma bubble drift velocities.

To compare the zonal drift velocities of the plasma bubbles with the thermospheric zonal wind velocities, we represent these velocities as v_{obs} (plasma bubbles), u_{eN} (winds at Chiang Mai), and u_{eS} (winds at Kototabang) in Table 4.1. In the table, positive values represent eastward velocities. Drift velocities were close to wind velocities at Kototabang at 1340 and 1510 UT, and were ∼20-

30 m/s larger than the wind at Kototabang after 1610 UT. Drift velocities were consistently ∼40-50 m/s larger than the wind at Chiang Mai. Drift velocities gradually decreased after 1510 UT, and from 1510 to 1730 UT the wind velocities at Kototabang rapidly decreased. Σ_{PN}, Σ_{PS}, v_{cal}, and v'_{cal} will be discussed in detail in Section 4.2.3.

Table 4.1: Observed and Calculated Parameters of Plasma Bubbles

UT	1340	1510	1610	1730	1820	1920
v_{obs} (m/s)	124	124	120	116	112	103
u_{eN} (m/s)		78	82			56
u_{eS} (m/s)	121	126	100	84	85	84
Σ_{PN} (S)	3.28	1.92	1.89	2.35	2.47	1.99
Σ_{PS} (S)	4.38	3.16	2.33	1.45	1.13	0.87
v_{cal} (m/s)		108	92			65
v'_{cal} (m/s)		102	91			70

Values of v_{obs} (eastward drift velocities of plasma bubbles), u_{eN} (eastward neutral winds at Chiang Mai), u_{eS} (eastward neutral winds at Kototabang), Σ_{PN} (field-line-integrated Pedersen conductivities at Chiang Mai), Σ_{PS} (field-line-integrated Pedersen conductivities at a conjugate point of Chiang Mai), v_{cal} (plasma bubble velocities estimated by using Σ_{PN}, Σ_{PS}, u_{eN}, and u_{eS}), and v'_{cal} (modified plasma bubble velocities by using F-region conductivities estimated from the ionosonde height profiles). Σ_{PN} and Σ_{PS} are integrated over altitudes between 200 and 400 km and calculated from the IRI and MSIS models.

4.2.2 F-region dynamo mechanism

Here, we introduce the F-region dynamo effect [e.g., *Rishbeth*, 1971] to discuss the relation between the drift velocities of the plasma bubbles and the velocities of the thermospheric zonal winds. In the nighttime ionosphere, the neutral wind, $\mathbf{u}$, generates an effective electric field as $\mathbf{u} \times \mathbf{B}$ by acting on the geomagnetic field, $\mathbf{B}$. The wind induces an ionospheric electric current, $\mathbf{j} = \sigma(\mathbf{E} + \mathbf{u} \times \mathbf{B})$, where $\mathbf{E}$ is the electric field and σ is the conductivity in the ionosphere. The electric field should be uniform along the geomagnetic field line. Considering that the conductivity in the E region is nearly zero at nighttime, we assume that the Pedersen current integrated along the geomagnetic field line in the F region is zero. We also assume that the observed winds are height independent in the F region. Then, the drift velocity of plasma bubbles, v_{cal}, which is represented as the background plasma drift velocity, is expressed as

$$v_{cal} = \frac{E}{B} = \frac{\Sigma_{PN}}{\Sigma_{PN} + \Sigma_{PS}} u_{eN} + \frac{\Sigma_{PS}}{\Sigma_{PN} + \Sigma_{PS}} u_{eS}, \tag{4.1}$$

where Σ_{PN} (Σ_{PS}) is the field-line-integrated conductivity of the F region in the northern (southern) hemisphere and u_{eN} (u_{eS}) is the observed thermospheric eastward winds in the northern (southern) hemisphere.

4.2.3 Comparison between calculated and observed bubble velocities

We described the calculated velocities of plasma bubbles as v_{cal} with the aim of expressing them as a function of thermospheric zonal winds and Pedersen conductivity in the F region in equation (4.1). The thermospheric zonal winds were obtained from the FPI observations. The field-line-integrated value of the Pedersen conductivity, Σ_{PN} and Σ_{PS} in equation (4.1), was calculated from the International Reference Ionosphere (IRI) [*Bilitza and Reinisch*, 2008] and Mass-Spectrometer-Incoherent-Scatter (MSIS) [*Picone et al.*, 2002] models. We used Σ_{PN} and Σ_{PS}, which are field-line-integrated values of the Pedersen conductivity, at Chiang Mai and at the conjugate point of Chiang Mai, respectively, along the field line over altitudes between 200 and 400 km. The values of Σ_{PN} and Σ_{PS}

at 1340, 1510, 1610, 1730, 1820, and 1920 UT are shown in Table 4.1. By using these values and the observed wind velocities, we calculated the plasma bubble velocity, v_{cal}, from equation (4.1). The obtained value of v_{cal} is also shown in Table 4.1. Note that we could not calculate v_{cal} at 1340, 1730, and 1920 UT because the wind velocities were not available owing to unfavorable sky conditions. The values of v_{obs} and v_{cal} were close for 1510 UT, indicating that most of the plasma drift velocities can be explained by the F-region dynamo mechanism. The difference between these values becomes larger as time passed.

The conductivity calculated above may not be the actual conductivity. Conductivity should be proportional to the neutral and plasma densities. If the altitudes of the F region increase, then the conductivity should decrease because neutral density decreases with increasing altitude. As shown in Figure 4.3(e), the virtual heights over Chiang Mai were higher than those over Kototabang, especially from 17 to 19 UT. However, due to the lack of wind observation at Chiang Mai, we could not calculate the value of v_{cal} at 1730 and 1820 UT when the heights are different at two stations. At 1510, 1610, 1920 UT, no height difference between the two stations was seen in Figure 4.3(e), indicating that actual Σ_{PN} and Σ_{PS} are nearly same. Considering that Σ_{PN} and Σ_{PS} are same, the bubble velocity is intermediate value of u_{eN} and u_{eS}, as shown in equation (4.1), at 1510, 1610, and 1920 UT when the wind velocity can be obtained at both hemispheres. The modified bubble velocities at these three times are shown as v'_{cal} in Table 4.1. The v'_{cal} is smaller than v_{cal} at 1510 and 1610 UT and larger at 1920 UT. However, even after this modification, the discrepancy between the calculated and observed velocities cannot be explained by only the F-region dynamo mechanism, because the observed velocity of plasma bubbles exceeded the observed wind velocities at both stations. If faster wind velocity exists near the dip equator at altitudes of ∼400-500 km (apex altitudes of the geomagnetic fields lines at conjugate stations over 250 km), the discrepancy may be explained, although the Pedersen conductivity decreases at higher altitudes in the F region. Actually, the wind speed at altitudes of ∼400 km around dip equator is larger than that in higher latitudes on the same geomagnetic field line [e.g., *Liu et al.*, 2009].

4.2.4 Possible causes of discrepancy between calculated and observed bubble velocities

Chapagain et al. [2013] have made comparison between nighttime thermospheric zonal neutral winds and plasma bubble drift velocities by using 1-year dataset in the western South American sector in the southern hemisphere. On several occasions, their observations showed that the plasma bubble velocities was larger than the neutral wind velocities, which has similar to our observations. They suggested that the discrepancy of the bubble-wind velocities is caused by the altitudinal gradient of plasma bubble velocity, because their measurement of bubble and neutral wind velocity were made at different latitudes. However, our present observation of bubble drift velocity and neutral wind was made at a same latitude, though we cannot measure altitudinal gradients.

Coley et al. [1994] statistically compared the zonal ion drift and the neutral winds in the ±35° MLAT range over all local times by using data from the ion drift meter and wind spectrometer aboard the DE-2 spacecraft. They showed that the eastward ion drift velocity was slightly larger than the eastward neutral wind velocity from 22 to 05 solar local time at ±5° MLAT, which is similar to what we found here. They suggested that this difference may be due to altitude gradients of neutral winds below 250 km, which can induce an additional polarization electric field and thus cause the observed larger velocity of ions than neutrals.

We estimated the drift velocities of the plasma bubbles from the 630-nm zonal keogram, as shown in Figures 4.3(a) and 4.3(b). We assumed that the 630-nm emission layer is at an altitude of 250 km in these keograms. This altitude is variable depending on the height profile of neutral and plasma densities. The velocity ambiguity would be $\sim \pm 20\%$ of the values shown in Table 4.1, because the peak altitude of the 630-nm airglow layer can vary from 200 to 300 km. If the airglow layer is at an altitude of 200 km, the values of v_{obs} at 1510, 1610, and 1920 UT are 98, 95, and 82 m/s, respectively. The values at 1510 and 1610 UT becomes similar to the values of v'_{cal}, while the value at 1920 UT are still larger than the values of v'_{cal}.

The velocity calculated from equation (4.1) does not include the effect of the

E region, because we assumed that the nighttime conductivity in the E region is much lower than that in the F region. Neglecting the E-region conductivity might cause the discrepancy between the calculated and observed velocities of the plasma bubbles. We can add a term of the E region in equation (4.1) to consider this effect. Usually the conductivity in the E region would be smaller than that in the F region. However, when the solar activity is low, the conductivity in the E region can become comparable to that in the F region at middle latitudes [e.g., *Ganguly et al.*, 1987]. If the E-region conductivity is equal to the F-region conductivity, the neutral wind velocity in the E region have to be larger than the F-region neutral wind to increase the calculated drift velocity in equation (4.1).

The plasma bubble velocities are obtained at Chiang Mai and conjugate point of Chiang Mai, while the wind data in the southern hemisphere is obtained at Kototabang which is geomagnetically equatorward of Chiang Mai. Here, we investigate the latitudinal difference of the zonal drift velocities of the observed plasma bubbles. Table 4.2 shows the values of the zonal drift velocities of plasma bubbles estimated from east-west keograms at two different latitudes; the first row shows the values at Kototabang (0.2°S) and conjugate point of Kototabang (15.9°N), and the second row shows those at conjugate point of Chiang Mai (3.0°S) and Chiang Mai (18.8°N), which is same as v_{obs} in Table 4.1. We determined these 4 v_{obs} independently using zonal keograms at these 4 latitudes. The velocities observed at the conjugate-pair latitudes were the same at all times. The observed zonal drift velocities at geomagnetically equatorward latitudes (first row) are slightly larger than those at geomagnetically poleward latitudes (second row), which is consistent with the previous study of plasma bubbles [e.g., *Sobral and Abdu*, 1991]. However, the latitudinal difference of the zonal drift velocity is very small and these observed bubble velocities anyhow exceeded the wind velocities in both hemispheres.

Table 4.2: Latitudinal Difference of Zonal Drift of Observed Plasma Bubbles

UT	1340	1510	1610	1730	1820	1920
v_{obs} (m/s) at 0.2°S and 15.9°N	128	124	124	120	112	109
v_{obs} (m/s) at 3.0°S and 18.8°N	124	124	120	116	112	103

4.3 Conclusions

We simultaneously observed plasma bubbles and the thermospheric neutral winds at Kototabang and Chiang Mai, which are nearly geomagnetically conjugate points. This is the first conjugate observations of plasma bubbles combined with the thermospheric winds at two hemispheres.

1. Plasma bubbles were observed in 630-nm airglow images at the two stations from 13 to 20 UT (from 20 to 03 LT) on 5 April 2011. The bubbles continuously propagated eastward with velocities of ∼100-125 m/s. The eastward velocities were same at the two stations and decreased as time passed.

2. Eastward neutral wind velocity in the thermosphere observed by FPIs at two stations also decreased as time passed. The wind velocities at Kototabang were larger than those at Chiang Mai.

3. The ionospheric virtual height observed by ionosondes was almost same at two stations except between 17 and 19 UT. The height over Chiang Mai were ∼20-30 km higher than that over Kototabang between 17 and 19 UT when the wind velocity could not be determined at Chiang Mai due to the sky condition.

4. The 630-nm images of Chiang Mai and those mapped to the conjugate point of Kototabang fit well, indicating that the observed plasma bubbles were geomagnetically connected at low latitudes.

5. To quantitatively assess the F-region dynamo effect, we compared the observed eastward drift velocities of plasma bubbles with the bubble velocities estimated from the observed neutral winds and the model conductivities obtained from the IRI and MSIS models at two conjugate points. The results show that the estimated drift velocities were ∼60-90% of the observed velocities of plasma bubbles, indicating that the thermospheric zonal wind velocities mostly dominate

the plasma drift velocities through the F-region dynamo effect.

6. The calculated plasma bubble velocities were 10-40% smaller than the observed velocities. This discrepancy may be caused by 1) faster neutral winds near the dip equator at altitudes higher than the 630-nm airglow layer, by 2) contribution from the conductivity and neutral winds in the E region, and by 3) the ambiguity of the bubble velocity estimation due to uncertainty of the peak altitude of the 630-nm airglow.

Chapter 5

Geomagnetically conjugate observations of ionospheric and thermospheric variations accompanied by a midnight brightness wave at low latitudes

Recent airglow observations have been used to investigate nighttime MSTIDs from low to high latitudes and plasma bubbles at equatorial and middle latitudes. *Otsuka et al.* [2004] conducted MSTID observations by airglow imagers at geomagnetically conjugate points in Japan and Australia at middle latitudes. They found that the nighttime MSTIDs at middle latitudes had symmetrical structures in both hemispheres and were connected by geomagnetic field lines. In Chapter 4, we conducted geomagnetically conjugate observations of plasma bubbles and thermospheric neutral winds at low-latitude conjugate stations. We indicated that the observed plasma bubble velocities were mostly determined by electric fields through the F-region dynamo mechanism. These observations indicate that the electric fields in the F region play important roles to create the characteristics of the observed ionospheric disturbances. In contrast, such a conjugate observation has not been conducted for the midnight brightness waves (MBWs).

In Chapter 5, we investigate the geomagnetic conjugacy of MBW using nighttime 630-nm airglow observations at two geomagnetically conjugate points at low latitudes. This is the first observations of MBW at geomagnetically conjugate points. We also investigate variations of thermospheric neutral winds and ionospheric heights accompanied by the MBW by using an FPI and ionosondes at the conjugate points.

5.1 Observations

Figures 5.1(a)-5.1(d) and 5.1(e)-5.1(h) show the 630-nm all-sky images acquired by the imagers at Kototabang and Chiang Mai, respectively, from 1602 to 1732 UT (from 2302 to 0032 LT) on 7 February 2011. The field-of-view of the imager is ∼500 km, which is shown by black circles in Figure 2.1. As shown in Figures 5.1(b) and 5.1(c), the airglow intensity is enhanced at 1632 and 1702 UT at Kototabang, showing a wave phase front elongated from southeast to northwest. This enhanced airglow structure is considered as an MBW because it propagated geomagnetically poleward only once at around the local midnight. On the other hand, the wave-like structure was not seen in the images of Chiang Mai as shown in Figures 5.1(e)-5.1(h). The enhanced airglow in the eastern and southern edges in Figures 5.1(e)-5.1(h) is due to city lights which come from the eastern edge and are reflected by a dome of the co-located FPI in the southern edge.

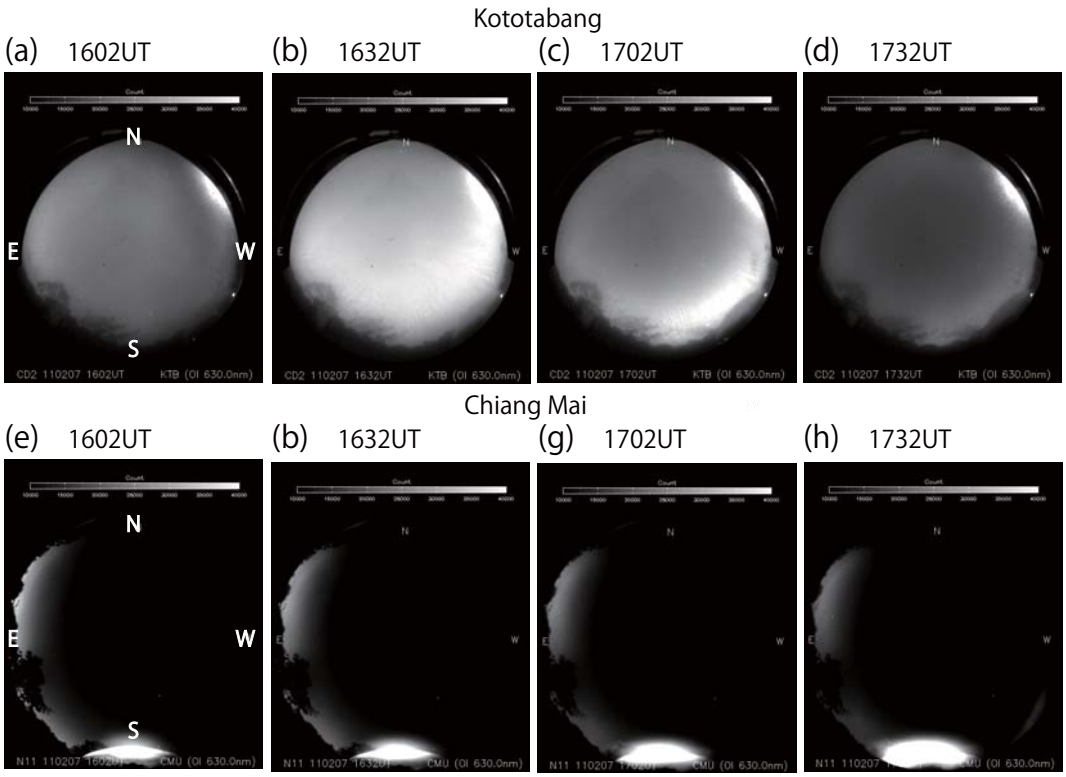

Figure 5.1: All-sky images obtained by airglow imagers at (a)-(d) Kototabang and (e)-(h) Chiang Mai from 1602 to 1732 UT on 7 February 2011. Up is geographic north and left is geographic east in each image.

Figures 5.2(a)-5.2(h) show the 630-nm airglow images at Kototabang, which are converted into geographic coordinates from all-sky coordinates. For the coordinate conversion, we assume that the 630-nm airglow emission layer is located at an altitude of 250 km. Note that the left is west and top is north, which is zonally opposite to Figure 5.1. The airglow intensity is represented in the absolute value as a unit of R. Between 1548 and 1618 UT, the airglow intensity in northeast of Kototabang (longitudes of 100-105°E and latitudes of 1°S-3°N) increases to ∼400 R. Then, a wave structure with a phase front elongated from west-northwest (WNW) to east-southeast (ESE) was seen between 1632 UT and 1718 UT, indicating a passage of an MBW over Kototabang. This MBW seems to propagate from the zenith to southwestern edge of the images. The airglow intensity inside the MBW is 200-600 R.

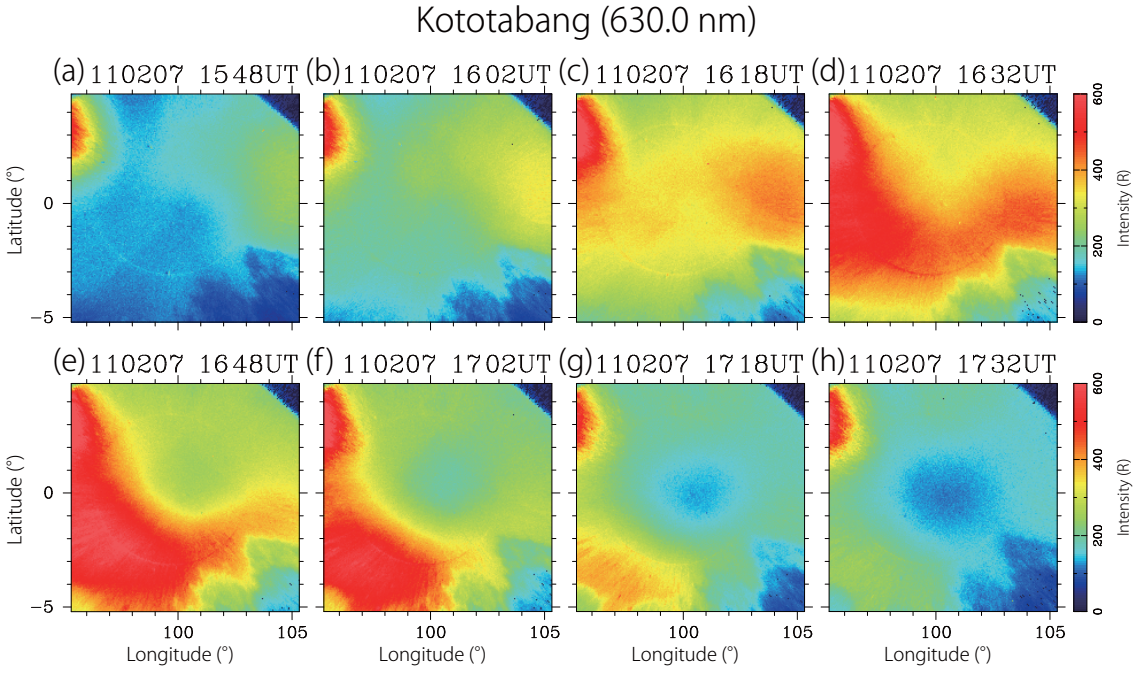

Figure 5.2: Two-dimensional 630-nm airglow images from 1548 to 1732 UT on 7 February 2011 at Kototabang represented as absolute airglow intensity in R. These images are converted from all-sky coordinates to geographic coordinates.

Figures 5.3(a)-5.3(h) show the 630-nm airglow images at Chiang Mai, which are converted into geographic coordinates from all-sky coordinates. The format is the same as Figure 5.2, while the airglow intensity is represented as the raw CCD counts, because the absolute intensity could not be calculated for the data of Chiang Mai due to a strong city-light contamination. The airglow intensity was less than 20000 counts and was stable in these 8 panels in Figure 5.3 with no discernible wave structures. The high airglow intensity in the eastern and southern edges of the images is due to the strong city-light contamination.

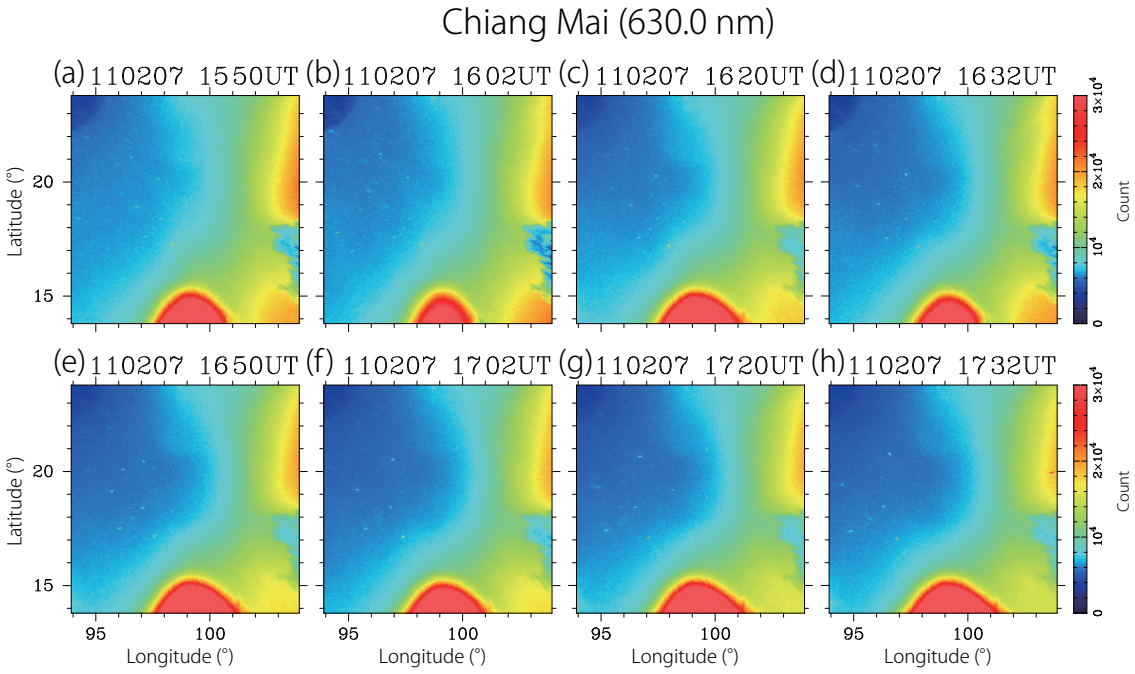

Figure 5.3: Two-dimensional 630-nm airglow images from 1550 to 1732 UT on 7 February 2011 at Chiang Mai represented as raw CCD counts. These images are converted from all-sky coordinates to geographic coordinates.

To estimate the observed wave velocity, we took zonal and meridional keograms of the 630-nm airglow images at a fixed latitude and longitude where the wave was clearly seen. Figures 5.4(a) and 5.4(b) show meridional and zonal keograms of Kototabang at a longitude of 97.0°E and a latitude of 3.0°S (defined as point A) on 7 February 2011, respectively. A southward-moving structure with intensities of 200-600 R was seen from 1540 to 1730 UT as shown in Figure 5.4(a), indicating the passage of an MBW. This MBW structure also slightly moved westward as shown in Figure 5.4(b). Thus, the propagation direction of the wave determined by these keograms was south-southwestward. The horizontal velocity of the MBW was ∼290 m/s.

Figures 5.5(a) and 5.5(b) show meridional and zonal keograms of Chiang Mai at a longitude of 96.6°E and a latitude of 18.9°N on 7 February 2011, respectively. These latitude and longitude are conjugate of point A. Note that the airglow intensity is again represented as the raw CCD counts as Figure 5.3. The moving structures were not seen in Figures 5.5(a) and 5.5(b), indicating that the conjugate MBW was not observed at Chiang Mai on this night. The airglow intensity above 101°E in Figure 5.5(b) is more than 10000 counts due to the city light.

Figures 5.4(c) and 5.4(d) show the northward and eastward thermospheric wind velocities observed by the FPI at Kototabang on 7 February 2011, respectively. Unfortunately, the FPI operation at Chiang Mai was stopped on this night. The mean values measured from 10 fringes of the Kototabang data are plotted with the error bar of the standard deviations. The error bars before 1530 UT are significantly large, because the airglow intensity was weak before 1530 UT. Both eastward and northward wind velocities are determined with small error bars after 1530 UT. The northward wind velocity started to decrease and turned to southward after 1530 UT in Figure 5.4(c). The southward wind velocity became largest (∼50 m/s) between 1650 and 1720 UT when the MBW was observed in the 630-nm images. The eastward wind velocity was 50-90 m/s and gradually decreased after 1530 UT. The wind direction was approximately eastward before the appearance of the MBW. Then, it turned to southeastward when the MBW appeared.

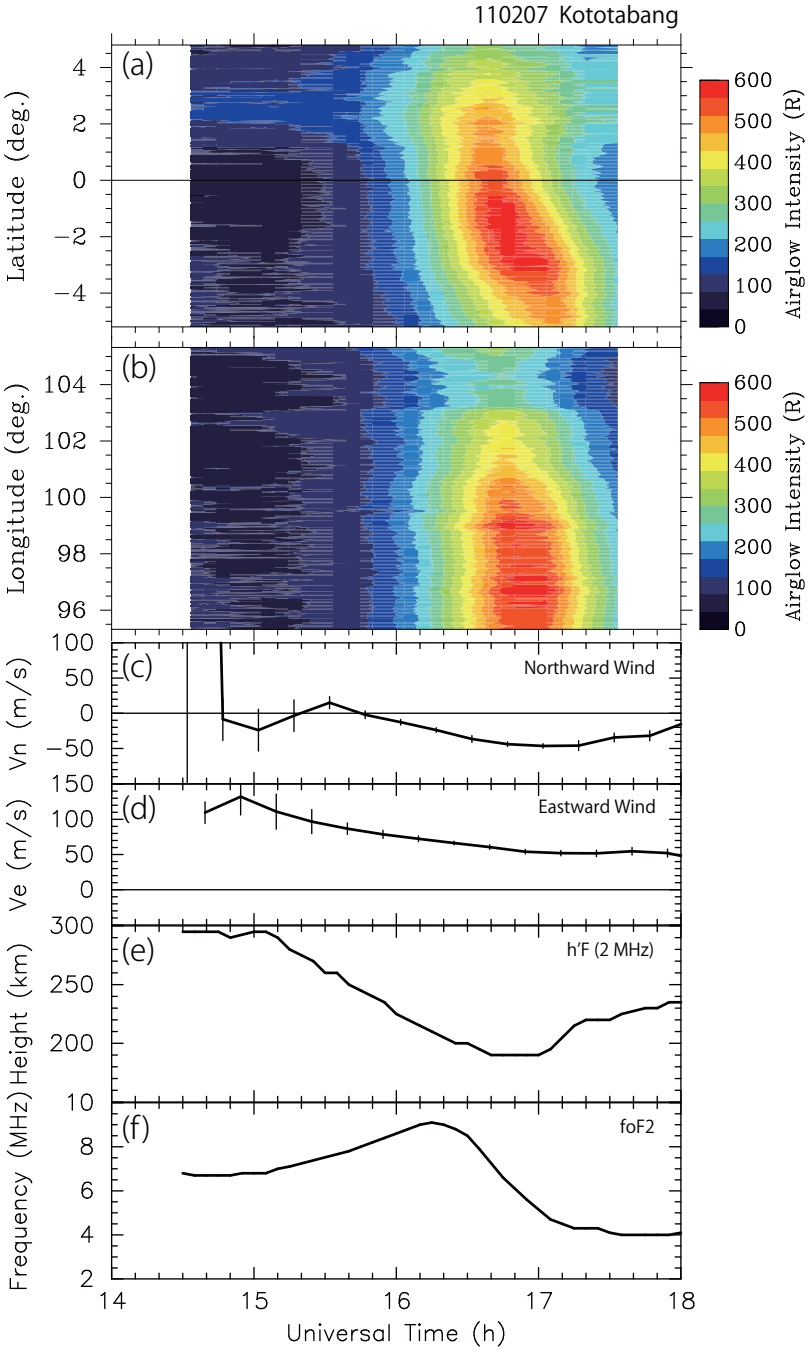

Figure 5.4: The 630-nm (a) meridional and (b) zonal keograms represented as absolute airglow intensity, averages and standard deviations of (c) northward and (d) eastward neutral wind velocities observed by an FPI, (e) virtual heights ($h'F$) at a frequency of 2 MHz and (f) F2-region critical frequency (f_oF_2) observed by an ionosonde, at Kototabang on 7 February 2011.

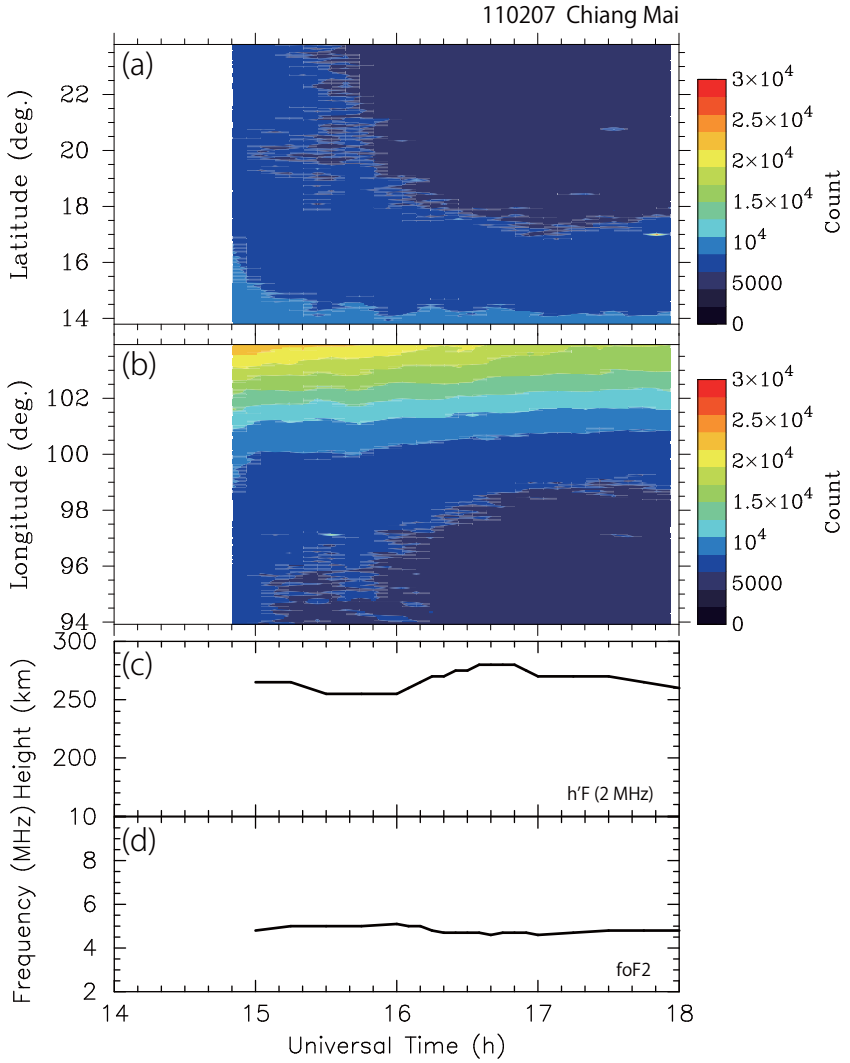

Figure 5.5: The 630-nm (a) meridional and (b) zonal keograms represented as raw CCD counts, (c) $h'F$ at a frequency of 2 MHz and (d) f_oF_2 observed by an ionosonde, at Chiang Mai on 7 February 2011.

Figures 5.4(e) and 5.5(c) show the ionospheric virtual heights ($h'F$) observed by the ionosondes at Kototabang and Chiang Mai, respectively. These values were obtained from ionograms at a frequency of 2 MHz which corresponds to a radio-wave frequency reflected at the bottomside F region. The height over Kototabang rapidly decreased from 300 km at 1500 UT to 190 km at 1640 UT before and during the airglow enhancement and increased from 190 km at 1700 UT to 240 km at 1800 UT after the airglow enhancement. The height was lowest when the airglow intensity became maximum between 1640 and 1700 UT. On the other hand at Chiang Mai, the height slightly increased from 250 km at 1600 UT to 280 km at 1640 UT, when the MBW was observed at Kototabang.

Figures 5.4(f) and 5.5(d) show the F2-region critical frequency (f_oF_2) observed by the ionosondes at Kototabang and Chiang Mai, respectively. These frequencies obtained from ionograms correspond to the plasma density at the F2-region peak. The value of f_oF_2 at Kototabang gradually increased before 1620 UT and rapidly decreased between 1620 and 1720 UT. The decrease of the observed f_oF_2 coincides with the MBW passage. On the other hand, clear f_oF_2 variation was not seen at Chiang Mai.

5.2 Discussion

5.2.1 Summary of the conjugate observations

We observed the wave-like airglow enhancement, probably corresponding to an MBW, at Kototabang, Indonesia, which propagated south-southwestward (geomagnetically poleward) with a horizontal velocity of ∼290 m/s. This wave was observed from 1540 to 1730 UT (from 2240 to 0030 LT) in the local midnight sector. The airglow intensity inside the MBW is 200-600 R, which is much larger than the background 630-nm airglow intensity before the MBW appearance. The observed wave is considered as an MBW, because it has just one phase front moving poleward around the midnight. The phase velocity of the present MBW is similar to that observed in Peru [*Colerico et al.*, 1996] and Puerto Rico [*Mendillo et al.*, 1997].

The airglow observation was also conducted at Chiang Mai, Thailand, which is nearly geomagnetically conjugate point of Kototabang. Similar wave-like airglow enhancement was not observed at Chiang Mai when the MBW was observed at Kototabang. This is the first evidence that the MBW does not have geomagnetic conjugacy. This feature is different from MSTIDs and plasma bubbles which show clear geomagnetic conjugacy [e.g., *Otsuka et al.*, 2002; 2004].

5.2.2 Relation between the MBW generation and background ionospheric variations

The airglow enhancement of MBW observed at Kototabang is caused by the ionospheric height decrease as shown by the ionosonde observation in Figure 5.4. The possible mechanism that causes height decrease of the ionosphere are downward $\mathbf{E} \times \mathbf{B}$ drift and poleward thermospheric winds. If the observed airglow enhancement was caused by the downward $\mathbf{E} \times \mathbf{B}$ drift, the electric field is instantly projected onto the northern hemisphere along the geomagnetic field line. As a result, similar ionospheric height decrease and airglow enhancement should be observed in the northern hemisphere. However, the observed MBW does not have geomagnetic conjugacy. Thus, the MBW and associated ionospheric height decrease would not be caused by the electric field.

At the midnight sector at Kototabang, the meridional wind observed by the FPI usually tends to be northward (geomagnetically equatorward). In the present event, however, the meridional neutral wind at Kototabang was turned to southward (geomagnetically poleward) after 1540 UT. This poleward wind may be caused by the pressure increase inside the midnight temperature maximum (MTM) region [e.g., *Herrero and Meriwether*, 1980; *Colerico et al.*, 1996]. Both the poleward wind and gravitational diffusion make the ionospheric plasma moving downward along the geomagnetic field line. As the result, the ionospheric height must rapidly decrease and then the 630-nm airglow intensity increases.

The f_oF_2 frequency observed at Kototabang gradually increased from 1500 to 1620 UT, which coincides with the height decrease observed from 1500 to 1640 UT. Such relation between ionospheric height decrease and f_oF_2 frequency increase can be caused by an enhancement of poleward neutral winds by pushing

down the plasma along the geomagnetic field line [e.g., *Shiokawa et al.*, 2002]. When the ionospheric height was minimum between 1640 and 1700 UT, the observed f_oF_2 rapidly decreased. This f_oF_2 decrease after 1620 UT is probably caused by the decrease of plasma density at F-region peak due to recombination with the high-density neutrals at lower altitudes.

5.2.3 Possible causes of the simultaneous height increase in the northern hemisphere

When the MBW was observed at Kototabang, a small increase of the ionospheric height was observed at Chiang Mai by a co-located ionosonde as shown in Figure 5.5(c). Unfortunately, we do not know thermospheric neutral wind variation at Chiang Mai on this night, because FPI failed its operation. As described above, a poleward wind rapidly causes the ionospheric height decrease. An equatorward wind pushes the plasma to higher altitudes until it balances with the downward gravitational diffusion. Thus, a small equatorward wind enhancement may explain the observed small height increase at Chiang Mai. However, if this is the case, it is difficult to explain why the height increase at Chiang Mai was coincident with the MBW at Kototabang. In the remaining part of this section, we discuss another possible generation mechanism of the observed small height increase of the ionosphere at Chiang Mai by polarization electric field associated with the MBW.

Figure 5.6 shows the schematic picture of the possible ionospheric variations during the present MBW event. The thermospheric neutral wind, $\mathbf{u}$, was approximately southeastward at Kototabang when the MBW was observed, as shown by the FPI data in Figures 5.4(c) and 5.4(d). The neutral wind drives the ionospheric current, $\mathbf{J}$, which has a direction of $\mathbf{E} + \mathbf{u} \times \mathbf{B_z}$, where $\mathbf{B_z}$ is the vertical component of the geomagnetic field. The background electric field, $\mathbf{E}$, is assumed to be zero. Thus, the horizontal current flows southwestward due to southeastward $\mathbf{u}$. The Pedersen conductivity inside the MBW is larger than that outside the MBW, because the Pedersen conductivity is proportional to the product of both plasma and neutral densities and thus, to the 630-nm airglow intensity. Considering the current flows across the MBW, positive and negative space charges would be ac-

cumulated at the southern and northern boundaries of the MBW, respectively, due to the existence of spatial inhomogeneity of the Pedersen conductivity and to keep current continuity inside and outside of MBW. Due to this space charge, a polarization electric field, E_P, is generated in the direction anti-parallel to the current (northeastward).

This polarization electric field will be projected onto the northern hemisphere along the geomagnetic field line almost without attenuation. The projected electric field is southeastward. The eastward component of the electric field and northward component of the geomagnetic field generate upward $\mathbf{E} \times \mathbf{B}$ drift. This is a possible scenario why a small height increase was observed at Chiang Mai simultaneously with the MBW at Kototabang.

According to this scenario, we roughly estimate the value of the upward $\mathbf{E} \times \mathbf{B}$ drift in the northern hemisphere. The upward $\mathbf{E} \times \mathbf{B}$ drift, v_Z, in the northern hemisphere is expressed by the eastward component of the projected polarization electric field and the northward component of the geomagnetic field, as

$$v_Z = \frac{E_P \sin\theta_1}{B_N} = (1 - \frac{\Sigma_{out}}{\Sigma_{in}}) u \frac{B_Z}{B_N} \sin\theta_1, \tag{5.1}$$

where Σ_{in} and Σ_{out} are the height-integrated Pedersen conductivity inside and outside MBW, respectively, B_N is the northward component of geomagnetic field at Chiang Mai, and θ_1 is an angle formed by the direction of the projected polarization electric field and the south.

The height-integrated Pedersen conductivity, Σ_{in} and Σ_{out}, is nearly proportional to the 630-nm airglow intensity, therefore, Σ_{out}/Σ_{in}=100(R)/600(R). Since the projected polarization electric field is southeastward, the value of θ_1 is $\sim$45°. The B_Z at Kototabang and B_N at Chiang Mai (conjugate point of Kototabang) are 1.22×10^4 nT and 3.56×10^4 nT at an altitude of 250 km. The observed thermospheric neutral winds, u, at Kototabang was $\sim$71 m/s southeastward when the MBW was observed. Substituting these values into equation (5.1), we calculated v_Z as 14.2 m/s. The ionospheric height increase observed at Chiang Mai was $\sim$30 km for 40 minutes in Figure 5.5, giving a vertical velocity of 12.5 m/s. This value is comparable to that from equation (5.1). Thus, we suggest that the observed small height increase over Chiang Mai is caused by the polarization electric field

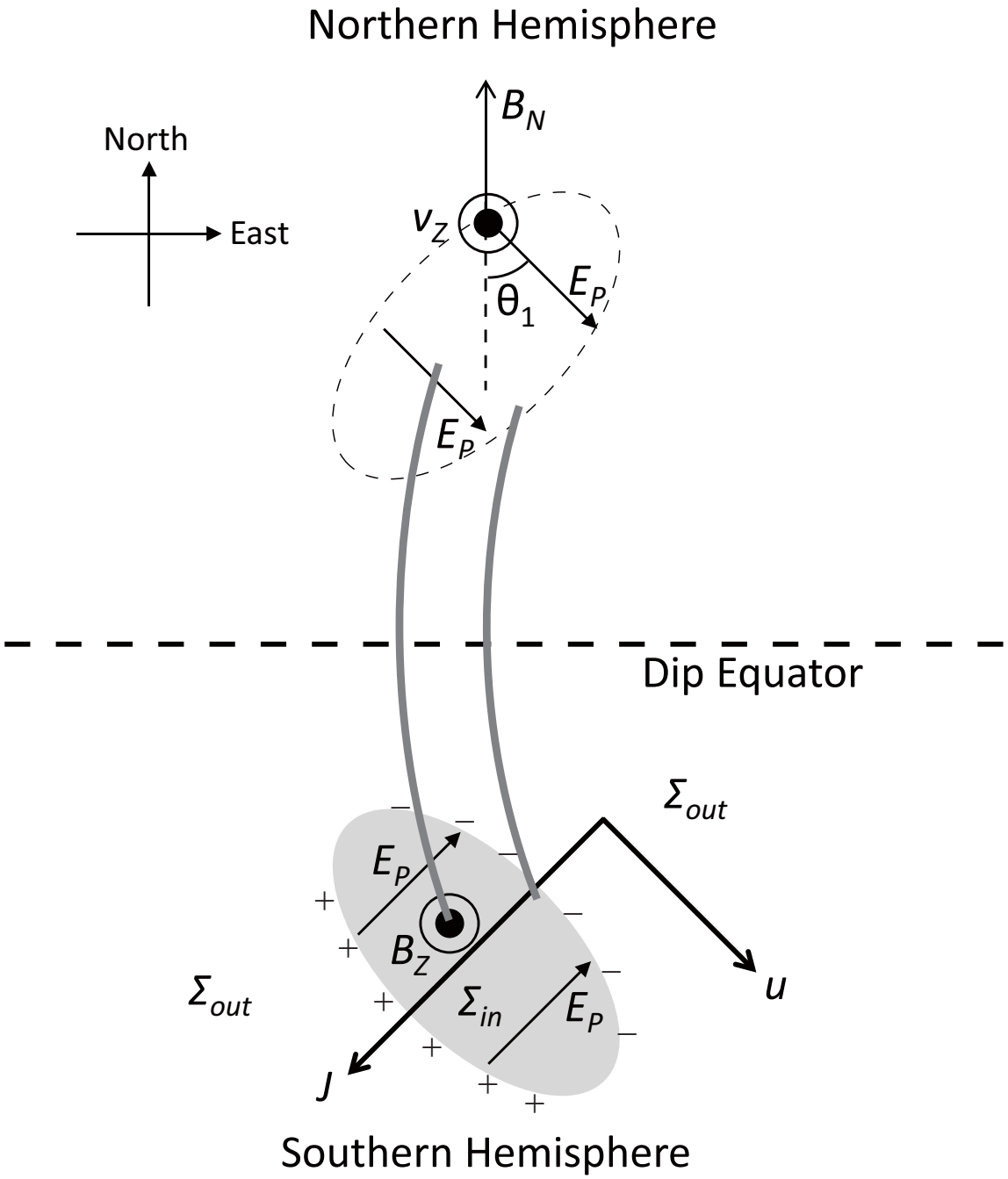

Figure 5.6: A schematic picture of the possible ionospheric variations during the MBW event on 7 February 2011. u is thermospheric neutral winds at Kototabang, J is an ionospheric current, E_P is a polarization electric field, B_Z and B_N are vertical and northward components of geomagnetic field, respectively, v_Z is an upward $\mathbf{E} \times \mathbf{B}$ drift, and Σ_{in} and Σ_{out} are height-integrated Pedersen conductivities inside and outside MBW, respectively.

projected from the MBW in the southern hemisphere.

5.3 Conclusions

We observed nighttime 630-nm airglow at Kototabang, Indonesia and Chiang Mai, Thailand which are nearly geomagnetically conjugate stations at low latitudes ($\sim$10°MLAT). The enhancement of the 630-nm airglow intensity of 200-600 R was observed from 1540 to 1730 UT (from 2240 to 0030 LT) on 7 February 2011 at Kototabang. This airglow enhancement is considered to be an MBW, because it was observed around local midnight and propagated geomagnetically poleward only once. The MBW has an ESE-WNW phase front and propagated south-southwestward with horizontal velocity of $\sim$290 m/s. However, similar MBW structure was not observed at Chiang Mai, indicating that the observed MBW did not have geomagnetic conjugacy. The poleward neutral wind observed by the FPI and the ionospheric virtual height observed by the ionosonde at Kototabang increased from -20 (northward) to 50 m/s (southward) and decreased from 300 to 190 km, respectively, when the MBW was observed. This southward wind is probably generated by the pressure increase inside the MTM. We suggested that southward (poleward) neutral wind moves plasma down to lower altitudes to cause the airglow enhancement observed as an MBW. When the MBW was observed at Kototabang, the ionospheric height slightly increased at Chiang Mai by $\sim$30 km. We suggest that the polarization electric field projected from the MBW in the southern hemisphere generated upward $\mathbf{E} \times \mathbf{B}$ drift in the northern hemisphere at Chiang Mai.

Chapter 6

General conclusions

In this thesis, we have studied equatorial and low-latitude ionospheric disturbances through the OI (630-nm) nighttime airglow observations. We continuously made imaging observations of the 630-nm nighttime airglow by using all-sky imagers at Kototabang, Indonesia (GLON: 100.3°E, GLAT: 0.2°S, and MLAT: 10.6°S) from October 2002 and at Chiang Mai, Thailand (GLON: 98.9°E, GLAT: 18.8°N, and MLAT: 8.9°N) from February 2010. Medium-scale traveling disturbances (MSTIDs), plasma bubbles, and midnight brightness waves (MBWs) observed in the 630-nm airglow images were reported. We also analyzed the background ionospheric conditions by observing thermospheric neutral winds and ionospheric heights at both stations during these events.

In Chapter 3, we statistically analyzed the MSTIDs observed at Kototabang, over 7 years from October 2002 to October 2009, to find their dependence on solar activities. From the 7-year statistics, we found that the occurrence rate and the average horizontal wavelength of the observed MSTIDs decreased and increased, respectively, with decreasing solar activity. Southward-moving MSTIDs were dominantly observed throughout 7 years. These results are consistent with the idea that the observed MSTIDs are caused by gravity waves in the thermosphere. The 46% of the observed MSTIDs would be caused by the secondary gravity waves generated in the thermosphere, since their phase speeds, v_{ph}, are larger than the sound speed ($\sim$300 m/s) in the lower atmosphere. We also compared the propagation directions of the observed MSTIDs with the locations of the tropospheric convection activity identified by cloud-top temperature, to find

the tropospheric sources of the MSTIDs. Strong tropospheric convection was found in the MSTID source direction for the 81% of the MSTIDs with $v_{ph} \leq 300$ m/s which could exist as gravity waves in the lower atmosphere. We suggest that primary gravity waves generated from the tropospheric convection propagate into the thermosphere and produce the observed MSTIDs for these cases.

In Chapter 4, we firstly analyzed zonal drift velocities of plasma bubbles and thermospheric neutral winds simultaneously observed at Kototabang and Chiang Mai, which are nearly geomagnetically conjugate points, to investigate how the F-region dynamo process affects the plasma drift. The plasma bubbles were observed in 630-nm airglow images at two stations from 13 to 20 UT (from 20 to 03 LT) on 5 April 2011 and continuously propagated eastward. The observed plasma bubbles have geomagnetic conjugacy. Thermospheric eastward neutral winds were also observed at two stations by co-located FPIs. Considering the F-region dynamo effects, we calculated the drift velocities of plasma bubble from the observed wind velocities and modeled conductivity. The results show that the calculated bubble drift velocities were 60-90% of the observed bubble drift velocities, indicating that the thermospheric zonal wind velocities mostly dominate the plasma drift velocities through the F-region dynamo effect. However, the calculated bubble drift velocities were 10-40% smaller than the observed velocities. This discrepancy may be caused by faster neutral winds near the dip equator at altitudes higher than the 630-nm airglow layer, by contribution from the conductivity and neutral winds in the E region, and by the ambiguity of the bubble velocity estimation due to uncertainty of the peak altitude of the 630-nm airglow.

In Chapter 5, we conducted geomagnetically conjugate airglow observations for an MBW at Kototabang and Chiang Mai, to investigate the geomagnetic conjugacy of the MBW. An airglow enhancement, which is considered as the MBW, was observed on 7 February 2011 at Kototabang. The MBW was observed at 1540-1730 UT (2240-0030 LT) around the local midnight and propagated south-southwestward with a velocity of 290 m/s. The poleward neutral wind increased and ionospheric height decreased when the MBW was observed. We suggest that the airglow enhancement was generated by the observed poleward neutral wind by pushing plasma along the geomagnetic field line. Similar airglow enhance-

ment was not observed at Chiang Mai, indicating that the MBW does not have geomagnetic conjugacy. Such an evidence of non-conjugacy of MBW was firstly reported by our present study. We also observed the ionospheric height over Chiang Mai to investigate the conjugate height variations accompanied by the MBW observed at Kototabang. The height observed at Chiang Mai slightly increased when the MBW was observed at Kototabang, although the MBW was not observed. We suggested that the polarization electric field projected from the MBW region of the southern hemisphere causes the observed small height increase at Chiang Mai.

From the above three studies, we can make the following statements: 1) Gravity waves in the thermosphere cause the nighttime MSTIDs at low latitudes. These gravity waves can be generated from the troposphere, and directly propagate into the thermosphere. 2) Plasma drift velocities are dominated by an electric field which is mainly generated by the thermospheric neutral winds through the F-region dynamo mechanism. 3) An MBW is generated by poleward thermospheric neutral winds and does not have geomagnetic conjugacy. These results indicate that the dynamics of the neutral atmosphere, i.e., gravity waves and thermospheric neutral winds, give dominant variations of the ionized atmosphere through neutral-plasma coupling processes. We conclude that dynamic variations of neutral atmosphere dominantly determine the characteristics of the ionospheric disturbances in the low-equatorial latitudes of the ionosphere.

For future studies of the ionospheric disturbances at low latitudes, we would conduct the geomagnetically conjugate observations of MSTIDs at Kototabang and Chiang Mai to investigate the conjugacy of the MSTIDs at low latitudes, because we did not see whether the low-latitude MSTIDs have symmetrical structures in both hemispheres as those observed at middle latitudes. Simultaneous observations of plasma bubbles and MSTIDs would be effective to investigate trigger of the plasma bubbles, because it was suggested that the inhomogeneity of the plasma densities, e.g., that by MSTIDs, at the bottom side of the F layer can grow up as plasma bubbles by the Rayleigh-Taylor instability. Simultaneous airglow-imaging observations of MSTIDs and mesospheric gravity waves can be used to investigate whether the MSTIDs are directly generated by gravity waves from the mesopause region.

References

Abalde, J. R., P. R. Fangundes, J. A. Bittencourt, and Y. Sahai (2001), Observations of equatorial *F* region plasma bubbles using simultaneous OI 777.4 nm and OI 630.0 nm imaging: New results, *J. Geophys. Res., 106(A12)*, 30331-30336, doi:10.1029/2001JA001115.

Abdu, M. A. (2001), Outstanding problems in the equatorial ionosphere-thermosphere electrodynamics relevant to spread F, *J. Atmos. Sol. Terr. Phys., 63(9)*, 869-884, doi:10.1016/S1364-6826(00)00201-7.

Bilitza, D., and B. W. Reinisch (2008), International Reference Ionosphere 2007: Improvements and new parameters, *Adv. Space Res., 42(4)*, 599-609, doi:10.1016/j.asr.2007.07.048.

Biondi, M. A., J. W. Meriwether, Jr., B. G. Fejer, S. A. Gonzalez, and D. C. Hallenbeck (1991), Equatorial thermospheric wind changes during the solar cycle: Measurements at Arequipa, Peru, from 1983 to 1990, *J. Geophys. Res., 96(A9)*, 15917-15930, doi:10.1029/91JA01645.

Bowman, G. G. (1990), A review of some recent work on midlatitude spread-*F* occurrence as detected by ionosondes, *J. Geomagn. Geoelectr., 42(2)*, 109-138.

Burke, W. J., L. C. Gentile, C. Y. Huang, C. E. Valladares, and S. Y. Su (2004), Longitudinal variability of equatorial plasma bubbles observed by DMSP and ROCSAT-1, *J. Geophys. Res., 109(A12)*, A12301, doi:10.1029/2004JA010583.

Brum, C. G. M., C. A. Tepley, J. T. Fentzke, E. Robles, P. T. dos Santos, and S. A. Gonzalez (2012), Long-term changes in the thermospheric neutral winds over Arecibo: Climatology based on over three decades of Fabry-Perot observations, *J. Geophys. Res., 117*, A00H14, doi:10.1029/2011JA016458.

Chapagain, N. P., J. J. Makela, J. W. Meriwether, D. J. Fisher, R. A. Buriti, and A. F. Medeiros (2012), Comparison of nighttime zonal neutral winds and equatorial plasma bubble drift velocities over Brazil, *J. Geophys. Res., 117*, A06309, doi:10.1029/2012JA017620.

Chapagain, N. P., D. J. Fisher, J. W. Meriwether, J. L. Chau, and J. J. Makela (2013), Comparison of zonal neutral winds with equatorial plasma bubble and plasma drift velocities, *J. Geophys. Res. Space Physics, 118*, 1802-1812, doi:10.1002/jgra.50238.

Colerico, M., M. Mendillo, D. Nottingham, J. Baumgardner, J. Meriwether, J. Mirick, B. W. Reinisch, J. L. Scali, C. G. Fesen, and M. A. Biondi (1996), Coordinated measurements of *F* region dynamic related to the thermospheric midnight temperature maximum, *J. Geophys. Res., 101*, 26783-26793.

Coley, W. R., R. A. Heelis, and N. W. Spencer (1994), Comparison of low-latitude ion and neutral zonal drifts using DE-2 data, *J. Geophys. Res., 99(A1)*, 341-348, doi:10.1029/93JA02205.

Farley, D. T., E. Bonelli, B. G. Fejer, and M. F. Larsen (1986), The prereversal enhancement of the zonal electric field in the equatorial ionosphere, *J. Geophys. Res., 91(A12)*, 13723-13728, doi:10.1029/JA091iA12p13723.

Fejer, B. G., E. Kudeki, and D. T. Farley (1985), Equatorial F region zonal plasma drifts, *J. Geophys. Res., 90(A12)*, 12249-12255, doi:10.1029/JA090iA12p12249.

Fejer, B. G., E. R. de Paula, S. A. Gonzalez, and R. F. Woodman (1991), Average vertical and zonal F region plasma drifts over Jicamarca, *J. Geophys. Res., 96(A8)*, 13901-13906, doi:10.1029/91JA01171.

Fukushima, D. (2012), Study of nighttime equatorial ionospheric disturbances in 630-nm airglow images, *Master Thesis, Nagoya University*.

Fukushima, D., K. Shiokawa, Y. Otsuka, and T. Ogawa (2012), Observation of equatorial nighttime medium-scale traveling ionospheric disturbances in 630-nm airglow images over 7 years, *J. Geophys. Res., 117*, A10324, doi:10.1029/2012JA017758.

Fukushima, D., K. Shiokawa, Y. Otsuka, M. Nishioka, M. Kubota, T. Tsugawa, T. Nagatsuma, S. Komonjinda, and C. Y. Yatini (2015), Geomagnetically conjugate observation of plasma bubbles and thermospheric neutral winds at low latitudes, *J. Geophys. Res.*, accepted.

Finlay, C. C., et al. (2010), International Geomagnetic Reference Field: the eleventh generation, *Geophys. J. Int., 183*, 1216-1230, doi:10.1111/j.1365-246X.2010.04804.x.

Ganguly, S., R. A. Behnke, and B. A. Emery (1987), Average electric field behavior in the ionosphere above Arecibo, *J. Geophys. Res., 92(A2)*, 1199-1210, doi:10.1029/JA092iA02p01199.

Garcia, F. J., M. C. Kelley, J. J. Makela, and C.-S. Huang (2000), Airglow observations of mesoscale low-velocity traveling ionospheric disturbances at midlatitudes, *J. Geophys. Res., 105(A8)*, 18407-18415, doi:10.1029/1999JA000305.

Greenspan, J. A. (1966), Synoptic description of the 6300 Å nightglow near 78° west longitude, *J. Atmos. Terr. Phys., 28*, 739-745.

Herrero, F. A., and J. W. Meriwether (1980), 6300-Å airglow meridional intensity gradients, *J. Geophys. Res., 85*, 4194-4204.

Hines, C. O. (1960), Internal atmospheric gravity waves at ionospheric heights, *Can. J. Phys., 38(11)*, 1441-1481.

Hooke, W. H. (1968), Ionospheric irregularities produced by internal atmospheric gravity waves, *J. Atmos. Terr. Phys., 30(5)*, 795-823, doi:10.1016/S0021-9169(68)80033-9.

Hunsucker, R. D. (1982), Atmospheric gravity waves generated in the high-latitude ionosphere, *Rev. Geophys. Space Phys., 20(2)*, 293-315, doi:10.1029/RG020i002p00293.

Ishida, T., K. Hosokawa, T. Shibata, S. Suzuki, N. Nishitani, and T. Ogawa (2008), SuperDARN observations of daytime MSTIDs in the auroral and mid-latitudes: Possibility of long-distance propagation, *Geophys. Res. Lett., 35(13)*, L13102, doi:10.1029/2008GL034623.

Johnston, J. E., and A. L. Broadfoot (1993), Midlatitude observations of the night airglow: Implications to quenching near the mesopause, *J. Geophys. Res., 98(A12)*, 21593-21603, doi:10.1029/93JA02318.

Kelley, M. C. (2009), The Earth's ionosphere, Second Edition, Plasma Physics and Electrodynamics, *Academic Press*, San Diego.

Kelley, M. C., and S. Fukao (1991), Turbulent upwelling of the mid-Latitude ionosphere, 2. Theoretical framework, *J. Geophys. Res., 96(A3)*, 3747-3753, doi:10.1029/90JA02252.

Kelley, M. C., and C. A. Miller (1997), Electrodynamics of midlatitude spread *F*, 3. Electrodynamic waves? A new look at the role of electric field in thermospheric wave dynamics, *J. Geophys. Res., 102(A6)*, 11539-11547, doi:10.1029/96JA03841.

Kotake, N., Y. Otsuka, T. Tsugawa, T. Ogawa, and A. Saito (2006), Climatological study of GPS total electron content variations caused by medium-scale traveling ionospheric disturbances, *J. Geophys. Res., 111*, A04306, doi:10.1029/2005JA011418.

Kotake, N., Y. Otsuka, T. Ogawa, T. Tsugawa, and A. Saito (2007), Statistical study of medium-scale traveling ionospheric disturbances observed with the GPS networks in Southern California, *Earth Planets Space, 59(2)*, 95-102.

Kubota, M., K. Shiokawa, M. K. Ejiri, Y. Otsuka, T. Ogawa, T. Sakanoi, H. Fukunishi, M. Yamamoto, S. Fukao, and A. Saito (2000), Traveling ionospheric disturbances observed in the OI 630-nm nightglow images over Japan by using a multi-point imager network during the FRONT campaign, *Geophys. Res. Lett., 27(24)*, 4037-4040, doi:10.1029/2000GL011858.

Kubota, M., M. Ishii, T. Tsugawa, J. Uemoto, H. Jin, Y. Otsuka, and K. Shiokawa (2009), New observational deployments for SEALION - Airglow measurements using all-sky imagers, *Journal of the National Institute of Information and Communications Technology, 56(1-4)*, 299-307.

Liu, H., S. Watanabe, and T. Kondo (2009), Fast thermospheric wind jet at the Earth's dip equator, *Geophys. Res. Lett., 36*, L08103, doi:10.1029/2009GL037377.

Makela, J. J., E. S. Miller, and E. R. Talaat (2010), Nighttime medium-scale traveling ionospheric disturbances at low geomagnetic latitudes, *Geophys. Res. Lett., 37*, L24104, doi:10.1029/2010GL045922.

Martinis, C., J. Baumgardner, J. Wroten, and M. Mendillo (2010), Seasonal dependence of MSTIDs obtained from 630.0 nm airglow imaging at Arecibo, *Geophys. Res. Lett., 37*, L11103, doi:10.1029/2010GL043569.

Maruyama, T., M. Kawamura, S. Saito, K. Nozaki, H. Kato, N. Hemmakorn, T. Boonchuk, T. Komolmis, and C. Ha Duyen (2007), Low latitude ionosphere-thermosphere dynamics studies with inosonde chain in Southeast Asia, *Ann. Geophys., 25(7)*, 1569-1577.

Mayr, H. G., I. Harris, N. W. Spencer, A. E. Hedin, L. E. Wharton, H. S. Porter, J. C. G. Walker, and H. C. Carlson Jr. (1979), Tides and the midnight temperature anomaly in the thermosphere, *Geophys. Res. Lett., 6(6)*, 447-450, doi:10.1029/GL006i006p00447.

Mendillo, M., and J. Baumgardner (1982), Airglow characteristics of equatorial plasma depletions, *J. Geophys. Res., 87*, 7641-7652, doi:10.1029/JA087iA09p07641.

Mendillo, M., J. Baumgardner, D. Nottingham, J. Aarons, B. Reinisch, J. Scali, and M. Kelley (1997), Investigations of thermospheric-ionospheric dynamics with 6300-Å images from the Arecibo Observatory, *J. Geophys. Res., 102(A4)*, 7331-7343, doi:10.1029/96JA02786.

Miller, C. A., W. E. Swartz, M. C. Kelley, M. Mendillo, D. Nottingham, J. Scali, and B. Reinisch (1997), Electrodynamics of midlatitude spread *F*, 1. Observations of unstable, gravity wave-induced ionospheric electric fields at tropical latitudes, *J. Geophys. Res., 102(A6)*, 11521-11532, doi:10.1029/96JA03839.

Nelson, G. J., and L. L. Cogger (1971), Dynamical behavior of the nighttime ionosphere at Arecibo, *J. Atmos. Terr. Phys., 33*, 1711-1726.

Ogawa, T., Y. Miyoshi, Y. Otsuka, T. Nakamura, and K. Shiokawa (2009), Equatorial GPS ionospheric scintillations over Kototabang, Indonesia and their relation to atmospheric waves from below, *Earth Planets Space, 61(4)*, 397-410.

Oliver, W. L., S. Fukao, M. Sato, Y. Otsuka, T. Takami, and T. Tsuda (1995), Middle and upper atmosphere radar observations of the dispersion relation for ionospheric gravity waves, *J. Geophys. Res., 100(A12)*, 23763-23768, doi:10.1029/95JA02520.

Otsuka, Y., K. Shiokawa, T. Ogawa, and P. Wilkinson (2002), Geomagnetic conjugate observations of equatorial airglow depletions, *Geophys. Res. Lett., 29(15)*, 1753, doi: 10.1029/2002GL015347.

Otsuka, Y., T. Kadota, K. Shiokawa, T. Ogawa, S. Kawamura, S. Fukao, and S.-R. Zhang (2003), Optical and radio measurements of a 630-nm airglow enhancement over Japan on 9 September 1999, *J. Geophys. Res., 102(A6)*, 1252, doi:10.1029/2002JA009594.

Otsuka, Y., K. Shiokawa, and T. Ogawa (2004), Geomagnetic conjugate observations of medium-scale traveling ionospheric disturbances at midlatitude using all-sky airglow imagers, *Geophys. Res. Lett., 31(15)*, L15803, doi:10.1029/2004GL020262.

Perkins, F. (1973), Spread *F* and ionospheric currents, *J. Geophys. Res., 78(1)*, 218-226, doi:10.1029/JA078i001p00218.

Picone, J. M., A. E. Hedin, D. P. Drob, and A. C. Aikin (2002), NRLMSISE-00 empirical model of the atmosphere: Statistical comparisons and scientific issues, *J. Geophys. Res., 107(A12)*, 1468, doi:10.1029/2002JA009430.

Rishbeth, H. (1971), Polarization fields produced by winds in the equatorial F-region, *Planet. Space Sci., 19*, 357-369, doi:10.1016/0032-0633(71)90098-5.

Röttger, J. (1977), Travelling disturbances in the equatorial ionosphere and their association with penetrative cumulus convection, *J. Atmos. Terr. Phys., 39(9-10)*, 987-998, doi:10.1016/0021-9169(77)90007-1.

Sagawa, E., T. Maruyama, T. J. Immel, H. U. Frey, and S. B. Mende (2003), Global view of the nighttime low-latitude ionosphere by the IMAGE/FUV 135.6 nm observations, *Geophys. Res. Lett., 30(10)*, 1534, doi:10.1029/2003GL017140.

Sahai, Y., P. R. Fagundes, and J. A. Bittencourt (2000), Transequatorial F-region ionospheric plasma bubbles: Solar cycle effects, *J. Atmos. Terr. Phys., 62(15)*, 1377-1383, doi:10.1016/S1364-6826(00)00179-6.

Saito, A., M. Nishimura, M. Yamamoto, S. Fukao, M. Kubota, K. Shiokawa, Y. Otsuka, T. Tsugawa, T. Ogawa, M. Ishii, T. Sakanoi, and S. Miyazaki (2001), Traveling ionospheric disturbances detected in the FRONT campaign, *Geophys. Res. Lett., 28(4)*, 689-692, doi:10.1029/2000GL011884.

Shiokawa, K., Y. Katoh, M. Satoh, M. K. Ejiri, T. Ogawa, T. Nakamura, T. Tsuda, and R. H. Wiens (1999), Development of optical mesosphere thermosphere imagers (OMTI), *Earth Planets Space, 51(7-8)*, 887-896.

Shiokawa, K., Y. Otsuka, T. Ogawa, N. Balan, K. Igarashi, A. J. Ridley, D. J. Knipp, A. Saito, and K. Yumoto (2002), A large-scale traveling ionospheric disturbance during the magnetic storm of 15 September 1999, *J. Geophys. Res., 107(A6)*, 1088, doi:10.1029/2001JA000245.

Shiokawa, K., Y. Otsuka, C. Ihara, T. Ogawa, and F. J. Rich (2003), Ground and satellite observations of nighttime medium-scale traveling ionospheric disturbance at midlatitude, *J. Geophys. Res., 108(A4)*, 1145, doi:10.1029/2002JA009639.

Shiokawa, K., Y. Otsuka, T. Ogawa, and P. Wilkinson (2004), Time evolution of high-altitude plasma bubbles imaged at geomagnetic conjugate points, *Ann. Geophys., 22(9)*, 3137-3143.

Shiokawa, K., Y. Otsuka, and T. Ogawa (2006), Quasiperiodic southward moving waves in 630-nm airglow images in the equatorial thermosphere, *J. Geophys. Res., 111*, A06301, doi:10.1029/2005JA011406.

Shiokawa, K., Y. Otsuka, and T. Ogawa (2009), Propagation characteristics of nighttime mesospheric and thermospheric waves observed by optical mesosphere thermosphere imagers at middle and low latitudes, *Earth Planets Space, 61(4)*, 479-491.

Shiokawa, K., Y. Otsuka, S. Oyama, S. Nozawa, M. Satoh, Y. Katoh, Y. Hamaguchi, Y. Yamamoto, and J. Meriwether (2012), Development of low-cost sky-scanning Fabry-Perot interferometers for airglow and auroral studies, *Earth Planets Space, 64(11)*, 1033-1046, doi:10.5047/eps.2012.05.004.

Sobral, J. H. A., and M. A. Abdu (1991), Solar activity effects on equatorial plasma bubble zonal velocity and its latitude gradient as measured by airglow scanning photometers, *J. Atmos. Terr. Phys., 53(8)*, 729-742, doi:10.1016/0021-9169(91)90124-P.

Sobral, J. H. A., H. Takahashi, M. A. Abdu, P. Muralikrishna, Y. Sahai, C. J. Zamlutti, E. R. de Paula, and P. P. Batista (1993), Determination of the quenching rate of the O(^{1}D) by O(^{3}P) from rocket-borne optical (630 nm) and electron density data, *J. Geophys. Res., 98(A5)*, 7791-7798, doi:10.1029/92JA01839.

Sobral, J. H. A., et al. (2009), Ionospheric zonal velocities at conjugate points over Brazil during the COPEX campaign: Experimental observations and theoretical validations, *J. Geophys. Res., 114*, A04309, doi:10.1029/2008JA013896.

Taylor, M. J., J.-M. Jahn, S. Fukao, and A. Saito (1998), Possible evidence of gravity wave coupling into the mid-latitude *F* region ionosphere during the SEEK campaign, *Geophys. Res. Lett., 25(11)*, 1801-1804, doi:10.1029/97GL03448.

Tsuda, T., and K. Hocke (2004), Application of GPS radio occultation data for studies of atmospheric waves in the middle atmosphere and ionosphere, *J. Meteor. Soc. Japan, 82(1B)*, 419-426, doi:10.2151/jmsj.2004.419.

Tsugawa, T., Y. Otsuka, A. J. Coster, and A. Saito (2007), Medium-scale traveling ionospheric disturbances detected with dense and wide TEC maps over North America, *Geophys. Res. Lett., 34(22)*, L22101, doi:10.1029/2007GL031663.

Vadas, S. L. (2007), Horizontal and vertical propagation and dissipation of gravity waves in the thermosphere from lower atmospheric and thermospheric sources, *J. Geophys. Res., 112*, A06305, doi:10.1029/2006JA011845.

Vadas, S. L., and G. Crowley (2010), Sources of the traveling ionospheric disturbances observed by the ionospheric TIDDBIT sounder near Wallops Island on 30 October 2007, *J. Geophys. Res., 115*, A07324, doi:10.1029/2009JA015053.

Vadas, S. L., and D. C. Fritts (2005), Thermospheric responses to gravity waves: Influences of increasing viscosity and thermal diffusivity, *J. Geophys. Res., 110*, D15103, doi:10.1029/2004JD005574.

Waldock, J. A., and T. B. Jones (1986), HF Doppler observations of medium-scale traveling ionospheric disturbances at mid-latitudes, *J. Atmos. Terr. Phys., 48(3)*, 245-260, doi:10.1016/0021-9169(86)90099-1.

Zhang, F. Q. (2004), Generation of mesoscale gravity waves in upper-tropospheric jet-front systems, *J. Atmos. Sci., 61(4)*, 440-457, doi:10.1175/1520-0469(2004).